

## Geochemistry, Geophysics, Geosystems

### RESEARCH ARTICLE

10.1002/2015GC005779

#### Special Section:

The Lithosphere-  
asthenosphere System

#### Key Points:

- The Tanzanian craton has one of the driest cratonic lithosphere yet analyzed
- Craton-plume interaction may not cause significant hydration of craton
- High T may be responsible for lowering the cratonic root viscosity at Labait

#### Supporting Information:

- Supporting Information S1
- Table S1
- Table S2
- Table S3
- Table S4

#### Correspondence to:

H. Hui,  
hhui@nju.edu.cn

#### Citation:

Hui, H., A. H. Peslier, R. L. Rudnick, A. Simonetti, and C. R. Neal (2015), Plume-cratonic lithosphere interaction recorded by water and other trace elements in peridotite xenoliths from the Labait volcano, Tanzania, *Geochim. Geophys. Geosyst.*, 16, doi:10.1002/2015GC005779.

Received 18 FEB 2015

Accepted 25 APR 2015

Accepted article online 29 APR 2015

## Plume-cratonic lithosphere interaction recorded by water and other trace elements in peridotite xenoliths from the Labait volcano, Tanzania

Hejiu Hui<sup>1,2,3</sup>, Anne H. Peslier<sup>4</sup>, Roberta L. Rudnick<sup>5</sup>, Antonio Simonetti<sup>2</sup>, and Clive R. Neal<sup>2</sup>

<sup>1</sup>State Key Laboratory for Mineral Deposits Research, School of Earth Sciences and Engineering, Nanjing University, Nanjing, China, <sup>2</sup>Department of Civil and Environmental Engineering and Earth Sciences, University of Notre Dame, Notre Dame, Indiana, USA, <sup>3</sup>Lunar and Planetary Institute, USRA-Houston, Houston, Texas, USA, <sup>4</sup>Jacobs, NASA Johnson Space Center, Houston, Texas, USA, <sup>5</sup>Department of Geology, University of Maryland, College Park, Maryland, USA

**Abstract** Water and other trace element concentrations in olivine (1–39 ppm H<sub>2</sub>O), orthopyroxene (10–150 ppm H<sub>2</sub>O), and clinopyroxene (16–340 ppm H<sub>2</sub>O) of mantle xenoliths from the Labait volcano, located on the edge of the Tanzanian craton along the eastern branch of the East African Rift, record melting and subsequent refertilization by plume magmas in a stratified lithosphere. These water contents are at the lower end of the range observed in other cratonic mantle lithospheres. Despite correlations between water content and indices of melting in orthopyroxene from the shallow peridotites, and in both olivine and orthopyroxene from the deep peridotites, water concentrations are too high for the peridotites to be simple residues. Instead, the Labait water contents are best explained as reflecting interaction between residual peridotite with a melt having relatively low water content (<1 wt.% H<sub>2</sub>O). Plume-derived melts are the likely source of water and other trace element enrichments in the Labait peridotites. Only garnet may have undergone addition of water from the host magma as evidenced by water content increasing toward the kelyphite rim in one otherwise homogeneous garnet. Based on modeling of the diffusion profile, magma ascent occurred at 4–28 m/s. In summary, plume-craton interaction appears to result in only moderate water enrichment of the lithosphere.

### 1. Introduction

Cratonic lithosphere remains stable over billion-year timescales, eluding destruction by tectonic processes and asthenospheric convection [e.g., Jordan, 1978; Walker *et al.*, 1989; O'Neill *et al.*, 2008]. Geologic processes such as continental rifting, however, may signal destabilization of the cratonic mantle lithosphere. The Archean Tanzanian craton [Chesley *et al.*, 1999; Burton *et al.*, 2000] is nestled between active branches of the East African Rift, which is the ultimate surface expression of one of the largest mantle upwellings detected on Earth (a so-called “super plume”), arising from the core-mantle boundary [e.g., Ritsema *et al.*, 1998; Nyblade *et al.*, 2000; Weeraratne *et al.*, 2003; Nyblade, 2011]. It is remarkable that the Tanzanian craton, despite its location, retains a deep (150–200 km) mantle cratonic root, as witnessed by xenocryst and xenolith thermobarometry [Griffin *et al.*, 1994; Chesley *et al.*, 1999; Lee and Rudnick, 1999] and seismic observations [Ritsema *et al.*, 1998; Weeraratne *et al.*, 2003; Adams *et al.*, 2012]. Although metasomatism by asthenosphere-derived melts linked to the super plume has been observed in Tanzanian craton xenoliths and xenocrysts [Cohen *et al.*, 1984; Dawson and Smith, 1988; Rudnick *et al.*, 1993, Griffin *et al.*, 1994; Rudnick *et al.*, 1994; Dawson, 1999; Lee and Rudnick, 1999; Rudnick *et al.*, 1999; Dawson, 2002; Aulbach *et al.*, 2008; Koornneef *et al.*, 2009; Aulbach *et al.*, 2011], their average density is lower than that of asthenospheric mantle and this appears to have been enough to counteract the negative buoyancy imposed by the cooler thermal state of cratonic lithospheric mantle [Lee and Rudnick, 1999; Gibson *et al.*, 2013], consistent with the isopycnic hypothesis of Jordan [1978].

Water is another key factor influencing the stability of cratonic lithosphere because of its role in controlling the viscosity of peridotite via the hydrolytic weakening of olivine [e.g., Mackwell *et al.*, 1985; Hirth and Kohlstedt, 1996; Mei and Kohlstedt, 2000a, 2000b; Dixon *et al.*, 2004; Li *et al.*, 2008; Peslier *et al.*, 2010; Lee *et al.*, 2011]. Nominally anhydrous, mantle minerals such as olivine, orthopyroxene, clinopyroxene, and garnet can

accommodate trace amounts of hydrogen, bonded to structural oxygen and generally associated with crystal lattice defects [e.g., *Keppler and Bolfan-Casanova*, 2006; *Smyth*, 2006]. These minerals typically contain a few to hundreds of ppm (by weight, and hereafter) H<sub>2</sub>O [e.g., *Bell and Rossman*, 1992a; *Peslier*, 2010]. Rheology of cratonic mantle is primarily controlled by its thermal state [e.g., *Karato and Wu*, 1993; *Lenardic et al.*, 2003; *Beuchert et al.*, 2010; *Lee et al.*, 2011], but low water contents in mantle minerals have also been proposed to contribute to the strength of cratonic lithosphere [e.g., *Pollack*, 1986; *Hirth and Kohlstedt*, 1996; *Dixon et al.*, 2004; *Li et al.*, 2008; *Peslier et al.*, 2010; *Lee et al.*, 2011]. Because water behaves incomparably during partial melting [e.g., *Michael*, 1995; *Aubaud et al.*, 2004; *Hauri et al.*, 2006; *Hirschmann*, 2006; *Kohn and Grant*, 2006; *Grant et al.*, 2007b; *Aubaud et al.*, 2008; *Tenner et al.*, 2009; *O'Leary et al.*, 2010], melting should deplete the residual peridotite in water, while metasomatism may enrich the lithospheric mantle in water [e.g., *Lee*, 2005; *Li et al.*, 2008; *Peslier et al.*, 2012; *O'Reilly and Griffin*, 2013; *Doucet et al.*, 2014].

Here we combine water contents with various tracers of melting and metasomatism for the Tanzanian cratonic mantle xenoliths (such as major and trace elements and radiogenic isotopes) [*Lee and Rudnick*, 1999; *Chesley et al.*, 1999; *Burton et al.*, 2000; *Aulbach et al.*, 2008; *Aulbach and Rudnick*, 2009; *Aulbach et al.*, 2011] to assess whether water plays a role in the preservation or destruction of cratonic mantle lithosphere [*Li et al.*, 2008; *Peslier et al.*, 2010, 2012; *Baptiste et al.*, 2012; *Doucet et al.*, 2014]. We present water contents of mantle xenoliths from Labait (Tanzania) and use these data, in conjunction with similar data for xenoliths from other northern Tanzanian xenolith localities [*Baptiste et al.*, 2015], to evaluate whether water played a role in cratonic mantle lithosphere stability in the presence of continental rifting resulting from a super plume.

## 2. Geologic Setting and Samples

The Tanzania craton is an amalgamation of several Archean greenstone belts, which were intruded by granites and migmatized during multistage tectono-metamorphic events [*Manya and Maboko*, 2003; *Manya et al.*, 2006; *Dawson*, 2008; *Manya and Maboko*, 2008; *Thomas et al.*, 2013; *Sanislav et al.*, 2014]. The craton is surrounded by several Proterozoic belts [*Möller et al.*, 1995; *Hanson*, 2003; *Tenczer et al.*, 2007]. Its northern margin has been reworked by the East African Rift and associated volcanism, which initiated at ~38 Ma in Ethiopia [*Dawson*, 2012]. The rift is associated with a thermal anomaly beneath eastern Africa that has been linked to an asthenospheric upwelling, sometimes called a “super plume”, as it may originate at the core-mantle boundary [e.g., *Ritsema et al.*, 1998; *Nyblade et al.*, 2000; *Weeraratne et al.*, 2003; *Nyblade*, 2011; *Hansen et al.*, 2012; *Wölbern et al.*, 2012; *Mulibio and Nyblade*, 2013]. The African superswell is one of the two largest mantle upwelling identified in the Earth's mantle [*McNutt*, 1998].

The Labait volcano is located on the eastern boundary of the Archean Tanzanian craton adjacent to the Mozambique Fold Belt. Labait has been dated to the Late Pleistocene based on U-Pb of metasomatic zircons from a phlogopite vein in a harzburgite xenolith [*Rudnick et al.*, 1999]. That vein is interpreted to have crystallized from East African Rift-related magmas that infiltrated ancient cratonic mantle lithosphere, prior to the entrainment of the xenolith in the host magma [*Rudnick et al.*, 1999].

Mantle xenoliths are abundant within the olivine-melilitites of the Labait volcano, with high proportions (~75%) of dense, Fe-rich dunites ( $Fo < 88$ ) in the xenolith population [*Lee and Rudnick*, 1999]. Residual peridotites make up ~22% of the xenoliths and the remaining 3% are crustal xenoliths [*Lee and Rudnick*, 1999]. The mantle lithosphere beneath Labait volcano is compositionally stratified [*Chesley et al.*, 1999; *Lee and Rudnick*, 1999]. The shallower part, to depths of ~130 km, is more refractory ( $0.33 < Al_2O_3 < 1.21$ ) and ancient (>2 Ga) based on Re depletion ( $T_{RD}$ ) ages [*Chesley et al.*, 1999; *Lee and Rudnick*, 1999; *Burton et al.*, 2000]. This shallow portion represents Tanzanian cratonic mantle lithosphere. Between ~130 and ~160 km, the peridotites are less refractory ( $0.41 < Al_2O_3 < 3.89$ ) and  $T_{RD}$  ages are <1 Ga [*Chesley et al.*, 1999; *Lee and Rudnick*, 1999]. These younger peridotites may represent lithosphere that formed at a later date, or Archean lithospheric mantle extensively overprinted by asthenosphere-derived melt or fluid linked to the super plume [*Chesley et al.*, 1999; *Lee and Rudnick*, 1999; *Aulbach et al.*, 2011]. Indeed, numerous lines of evidence indicate that multiple metasomatic events occurred in the Tanzanian cratonic mantle beneath Labait [*Chesley et al.*, 1999; *Lee and Rudnick*, 1999; *Rudnick et al.*, 1999; *Aulbach et al.*, 2008; *Koornneef et al.*, 2009; *Aulbach et al.*, 2011]. The Os, Sr, Nd, Li, and He isotope data collectively indicate that all mantle xenoliths from Labait

**Table 1.** Summary of Labait Mantle Xenolith Characteristics

| Sample                          | Lithology <sup>e</sup> | Texture <sup>a</sup>                | Modal Mineralogy <sup>b,e</sup> (%)   | T <sup>c</sup> (°C) | P <sup>c</sup> (GPa) | FeO <sup>b</sup> (wt%) | T <sub>RD</sub> <sup>a</sup> (Ga) | Fo <sup>b</sup> |
|---------------------------------|------------------------|-------------------------------------|---|---------------------|----------------------|------------------------|-----------------------------------|-----------------|
| <i>T<sub>RD</sub> &lt; 1 Ga</i> |                        |                                     |   |                     |                      |                        |                                   |                 |
| LB12                            | Grt Lherz              | fine-grained                        | Ol <sub>70.1</sub> Opx <sub>15.3</sub> Cpx <sub>7.0</sub> Grt <sub>7.6</sub>  | 1290                | 4.6                  | 8.34                   | 0.33                              | 90.6            |
| LB45 <sup>d</sup>               | Grt Lherz              | tabular-mosaic porphyroclastic      | Ol <sub>60.8</sub> Opx <sub>9.8</sub> Cpx <sub>14.0</sub> Grt <sub>15.4</sub> | 1410                | 4.9                  | 8.34                   | 0                                 | 90.2            |
| LB4                             | Grt Harz               | porphyroclastic                     | Ol <sub>68.2</sub> Opx <sub>22.5</sub> Cpx <sub>4.1</sub> Grt <sub>5.1</sub>  | 1320                | 4.1                  | 7.55                   | 0.34                              | 91.3            |
| LB50                            | Grt Harz               | fine-grained porphyroclastic        | Ol <sub>72.8</sub> Opx <sub>20.3</sub> Cpx <sub>2.5</sub> Grt <sub>4.4</sub>  | 1360                | 4.8                  | 7.76                   | 0.98                              | 91.2            |
| LB53                            | Grt Harz               | fine-grained mosaic porphyroclastic | Ol <sub>77.3</sub> Opx <sub>10.2</sub> Cpx <sub>5.1</sub> Grt <sub>7.5</sub>  | 1300                | 4.7                  | 7.93                   | 0.71                              | 91.1            |
| KAT17                           | Grt Harz               | foliated porphyroclastic            | Ol <sub>72.0</sub> Opx <sub>24.1</sub> Cpx <sub>3.5</sub> Grt <sub>0.4</sub>  | 1250                | 4.0                  | 10.55                  | 0.36                              | 89.0            |
| <i>T<sub>RD</sub> &gt; 2 Ga</i> |                        |                                     |   |                     |                      |                        |                                   |                 |
| LB24                            | Grt Harz               | coarse-grained                      | Ol <sub>76.9</sub> Opx <sub>17.6</sub> Cpx <sub>1.0</sub> Grt <sub>4.5</sub>  | 1270                | 4.4                  | 6.92                   | 2.20                              | 92.4            |
| LB34 <sup>d</sup>               | Phl Grt Harz           | coarse-grained porphyroclastic      | Ol <sub>88.2</sub> Opx <sub>8.2</sub> Cpx <sub>1.1</sub> Grt <sub>2.6</sub>   | 1120                | 3.2                  | 9.28                   | 2.48                              | 89.9            |
| LB1                             | Phl Chr Harz           | coarse-granular                     | Ol <sub>77.7</sub> Opx <sub>20.6</sub> Chr <sub>1.7</sub>                     |                     |                      | 6.38                   | 2.53                              | 92.1            |
| LB9 <sup>d</sup>                | Chr Harz               | coarse-granular                     | Ol <sub>76.7</sub> Opx <sub>13.4</sub> Cpx <sub>7.0</sub> Chr <sub>2.8</sub>  | 930                 | (2.5)                | 6.50                   | 2.49                              | 93.3            |
| LB11                            | Sp Harz                | fine-grained                        | Ol <sub>78.6</sub> Opx <sub>19.5</sub> Cpx <sub>0.8</sub> Sp <sub>1.2</sub>   | 1000                | (2.5)                | 7.18                   | 2.24                              | 92.3            |
| LB14 <sup>d</sup>               | Phl Harz               | fine-grained                        | Ol <sub>94.9</sub> Opx <sub>3.7</sub> Cpx <sub>1.7</sub>                      | 1100                | (4.5)                | 7.15                   | 2.80                              | 92.9            |

<sup>a</sup>The detailed texture descriptions of Labait mantle xenoliths can be found in Chesley et al. [1999]. T<sub>RD</sub> is the rhenium depletion age determined by Chesley et al. [1999].

<sup>b</sup>The modal mineralogy, whole-rock FeO content, and Fo are from Lee and Rudnick [1999].

<sup>c</sup>Equilibration temperatures and pressures were calculated using the two-pyroxene thermometer [Brey and Köhler, 1990] and Al-in-oxp barometer [Brey and Köhler, 1990] for garnet-bearing xenoliths; the two-pyroxene thermometer [Brey and Köhler, 1990] for garnet-free and clinopyroxene bearing samples with input pressures in parentheses following Lee and Rudnick [1999]. Temperature and pressure could not be calculated for the clinopyroxene-and-garnet-free sample LB1 due to the lack of a reliable thermobarometer for this mineral assemblage. Major element compositions of Labait mantle minerals used in these calculations are from Lee and Rudnick [1999].

<sup>d</sup>The clinopyroxene in LB45, LB34, LB9 and LB14 may be secondary (see text, also Lee and Rudnick [1999]).

<sup>e</sup>Grt = garnet, Chr = chromite, Sp = spinel, Phl = phlogopite, Ol = olivine, Opx = orthopyroxene, Cpx = clinopyroxene, Fo = forsterite content (Mg/(Mg+Fe)), Lherz = lherzolite, Harz = harzburgite.

were variously overprinted by metasomatic agents, the most recent of which are related to a mantle plume that has HIMU characteristics [Chesley et al., 1999; Aulbach et al., 2008, 2011].

The samples analyzed here are a subset of the peridotite xenoliths described in Lee and Rudnick [1999] and subsequently studied by Vauchez et al. [2005] for lattice preferred orientation, and Chesley et al. [1999] for Re-Os systematics. Three of the samples were also analyzed by Aulbach et al. [2008] for Sr, Nd, and Li isotopes and trace elements in clinopyroxene. Six of the samples studied here belong to the younger (<1 Ga) and deeper (4.0 – 4.9 GPa) group, while the other six are part of the older (>2 Ga) and shallower group ( $\leq 4.4$  GPa) (Table 1). The older group includes one spinel harzburgite, two chromite-bearing harzburgites, two garnet harzburgites and one dunite; three contain trace amounts of secondary (metasomatic) phlogopite (Table 1) [Lee and Rudnick, 1999]. All younger peridotites contain garnet and range from harzburgite to lherzolite (Table 1). One sample in each group (KAT17 and LB34, in the younger and older groups, respectively) is too Fe-rich (whole-rock FeO > 9 wt.% [Lee and Rudnick, 1999]; Table 1) for the major element composition to be simply explained by partial melting. This is illustrated by comparing the Labait peridotite Al<sub>2</sub>O<sub>3</sub> and FeO compositions to the experimentally determined peridotite melting curves of Herzberg [2004] (Figure 1a). The two Fe-rich samples do not plot near the melting curves and probably experienced Fe addition via metasomatism. These samples are porphyroclastic, as are garnet peridotites LB4, LB45, LB50 and LB53 (Table 1). Labait samples record higher equilibration temperatures and plot to the high-temperatures side of a typical cratonic geotherm [Lee and Rudnick, 1999; Selway et al., 2014], including those of the Kaapvaal and Siberian cratons, and even the xenoliths from nearby Lashaine, which occurs within the Mozambique Belt (Figure 2a).

### 3. Analytical Methods

Handpicked mineral grains of olivine, orthopyroxene, clinopyroxene, and garnet were embedded in epoxy and doubly polished into thick sections. Grain sizes vary from <1 mm up to ~5 mm. Orientation of olivine and pyroxene was obtained with interference figures under a petrographic microscope. Representative grains were analyzed using two different Fourier transform infrared (FTIR) spectrometers at NASA-Johnson Space Center: A Continuum microscope attached to a Nicolet NEXUS 670FT FTIR spectrometer, and later a newly installed Hyperion 3000 microscope attached to a Bruker Vertex 70. The water content was calculated using the integrated area beneath the OH vibration bands and the Beer-Lambert law with an integral absorption coefficient specific for olivine, orthopyroxene, clinopyroxene and garnet [Bell et al., 1995, 2003a];

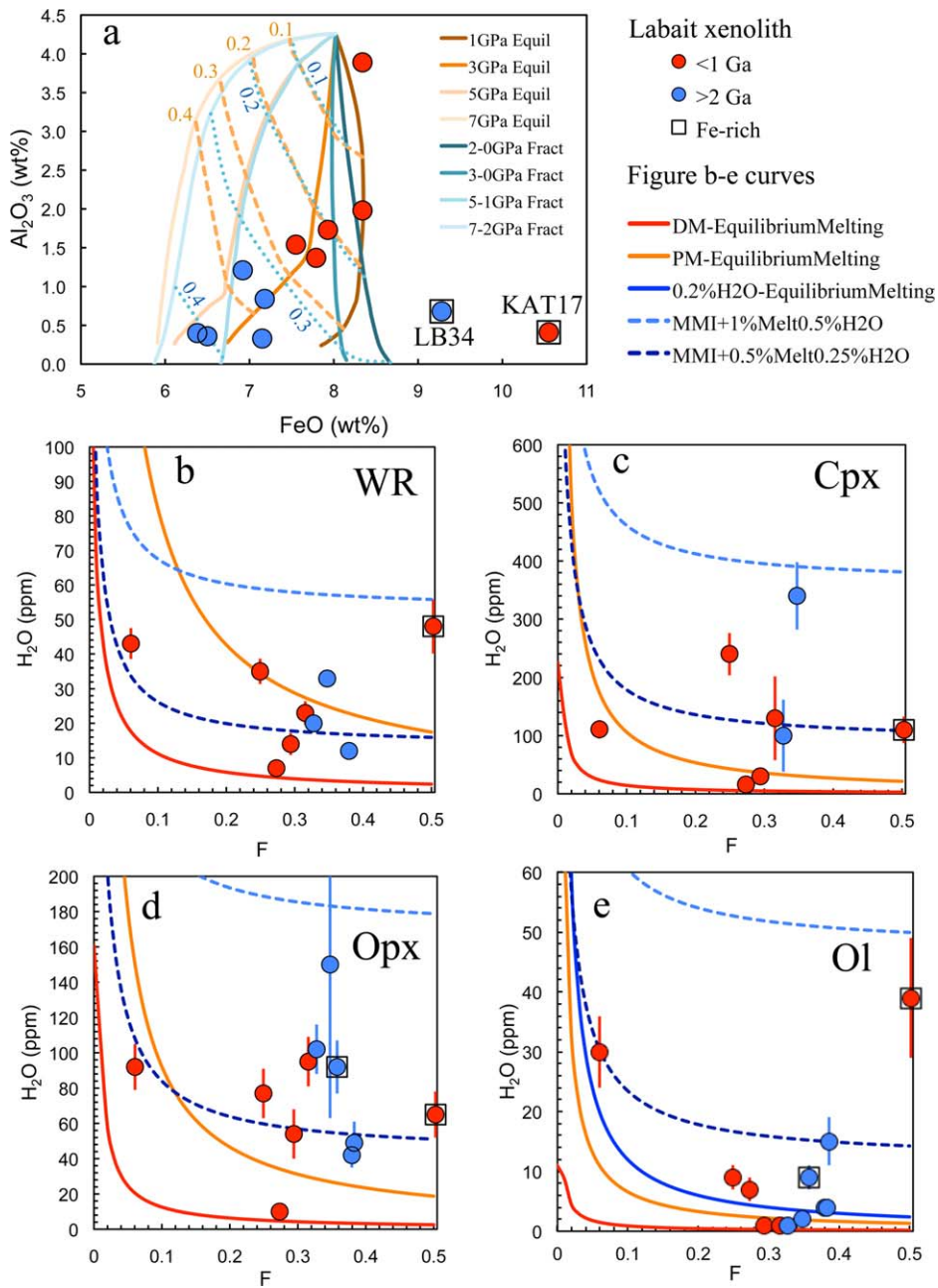


**Figure 1.** Melting and melt-rock interaction (MRI) models for the Labait peridotites. Numbered bold and dashed lines (Figure 1a) are experimental melting curves plotted in terms of whole-rock  $\text{FeO}$  and  $\text{Al}_2\text{O}_3$  for different pressures and melt fractions, respectively [Herzberg, 2004]. Lines in Figure 1b–e are equilibrium (Equil—solid lines) melting curves for depleted mantle (DM, 150 ppm  $\text{H}_2\text{O}$ ) [Michael, 1988; Dixon *et al.*, 2002], primitive mantle (PM, 1100 ppm  $\text{H}_2\text{O}$ ) [Palme and O'Neill, 2007] and a mantle source with 0.2 wt.%  $\text{H}_2\text{O}$  [Shaw, 1979], and equilibrium melting curves (dashed lines) for a DM source that interacted with 1% (or 0.5%) of melt (MRI) containing 0.5 (or 0.25) wt.%  $\text{H}_2\text{O}$  [DePaolo, 1981]. Details of the modeling can be found in the supporting information Text S1. The water contents of most peridotites and the Fe contents of a subset of peridotites are too high to be modeled by melting of a depleted or primitive mantle source. Mass fraction of melt for each sample ( $F$ ) was determined using the curves of Herzberg [2004]: the 4 GPa equilibrium melting curves for the younger peridotites, and the decompression fractional melting curve from 5 to 1 GPa for the older peridotites. Enrichment of the peridotites by Fe-rich silicate melts containing <1 wt.%  $\text{H}_2\text{O}$  best explains the data. Major-element compositions of Labait peridotites are from Lee and Rudnick [1999]. WR = whole rock, Ol = olivine, Opx = orthopyroxene, Cpx = clinopyroxene.

Withers *et al.*, 2012]. Systematic analyses at the core and edge of each olivine grain were performed to examine homogeneity of water contents. In addition, cross-sectional analyses on two olivine grains from two xenoliths were also carried out using an Autolimage microscope on a Perkin Elmer Spectrum GX FTIR at the University of Michigan.

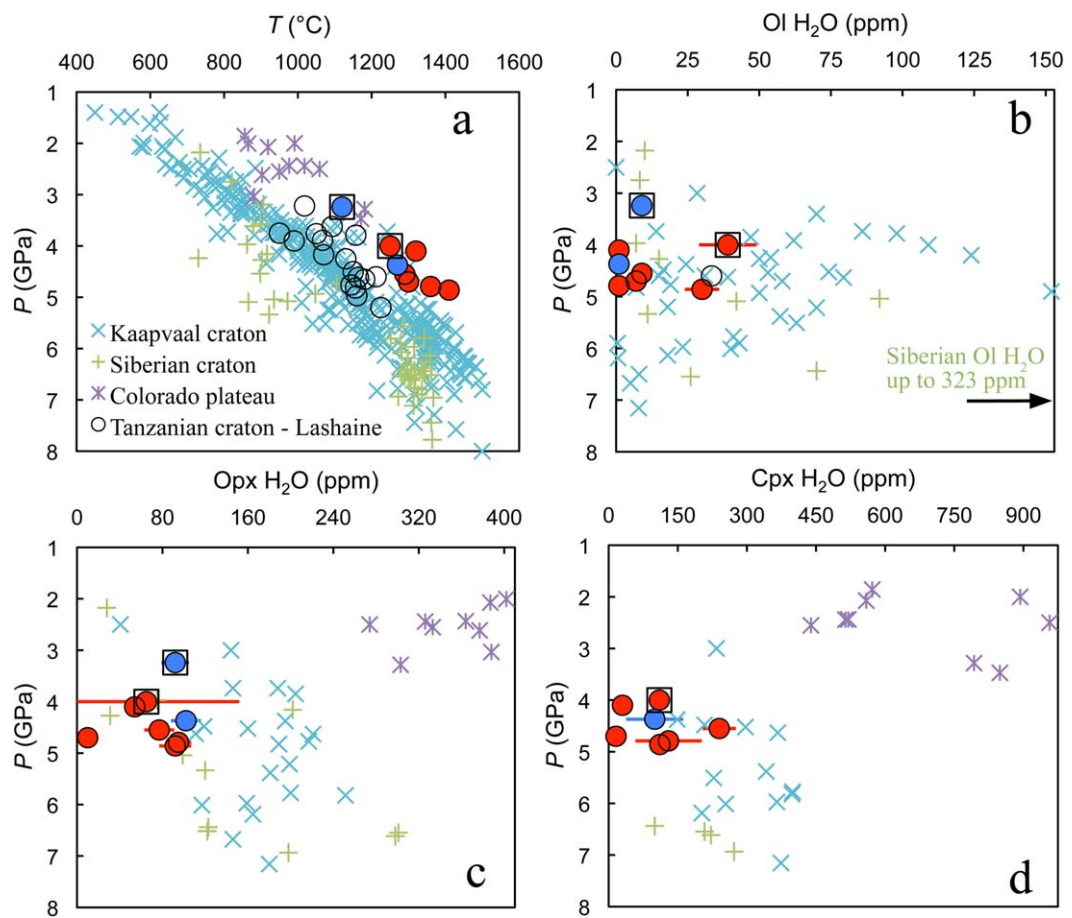


**Figure 2.** Equilibrium pressure versus (a) temperature, and (b) water content of olivine, (c) orthopyroxene, and (d) clinopyroxene for xenolithic peridotites from the Tanzanian craton (Labait, symbols as in Figure 1 (this study); Lashaine [Gibson et al., 2013; Baptiste et al., 2015]), Kaapvaal craton [Kurosawa et al., 1997; Bell et al., 2003b; James et al., 2004; Grant et al., 2007a; Peslier et al., 2008, 2010; Baptiste et al., 2012; Peslier et al., 2012], Siberian craton [Bell et al., 2003b; Ionov et al., 2010; Doucet et al., 2014], and Colorado plateau [Li et al., 2008]. The Labait peridotites are characterized by higher temperatures and lower water contents compared to those of the Kaapvaal and Siberian cratons [Peslier et al., 2012; Doucet et al., 2014].

In-situ trace element abundances of Labait pyroxene and garnet were obtained using a 213 nm Nd-YAG New Wave laser ablation system in conjunction with a Thermo-Finnigan Element 2 high resolution magnetic sector inductively coupled plasma mass spectrometry (LA-ICP-MS) in the Midwest Isotope and Trace Element Research Analytical Center (MITERAC) at the University of Notre Dame. Details of the methods, and comparison with published data [Aulbach et al., 2008] can be found in the supporting information Text S1.

## 4. Results

Detailed petrographic descriptions of the Labait mantle xenoliths have been reported previously [Chesley et al., 1999; Lee and Rudnick, 1999]. The samples are serpentine free and generally fresh [Lee and Rudnick, 1999], which is consistent with our microscopic observations of the minerals in the doubly polished mounts.

### 4.1. Olivine

The O-H bands of Labait xenolith olivines (Figure 3a) resemble those obtained for olivines of mantle xenoliths in other locations [e.g., Bell et al., 2003a; Matsyuk and Langer, 2004; Li et al., 2008; Yang et al., 2008; Peslier et al., 2010; Xia et al., 2010; Baptiste et al., 2015]. The O-H bands are pleochroic and located between  $3650$  and  $3450 \text{ cm}^{-1}$ . No OH bands are observed in the low wavenumber range ( $<3400 \text{ cm}^{-1}$ ), as are sometimes observed in olivine [e.g., Bell et al., 2003a; Matsyuk and Langer, 2004; Li et al., 2008; Baptiste et al., 2015]. The O-H bands obtained with the electric vector parallel to ( $E//\gamma$ ) have the strongest absorbance

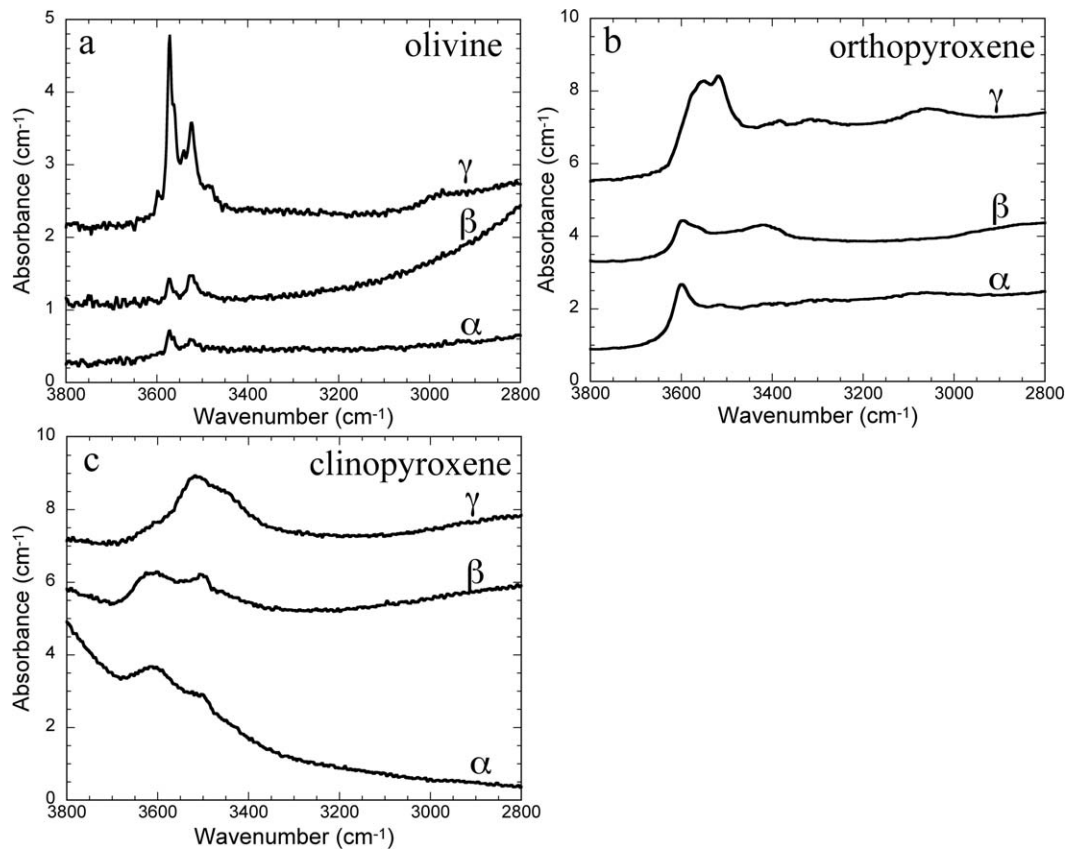


**Figure 3.** Representative polarized FTIR absorption spectra for (a) olivine, (b) orthopyroxene, and (c) clinopyroxene from Labait mantle xenoliths normalized to 1 cm thickness in the O-H vibration region. Spectra for three perpendicular orientations ( $\alpha$ ,  $\beta$ , and  $\gamma$ ) are shifted vertically to allow comparison.

relative to those with  $E//\alpha$  and  $\beta$  (Figure 3a and Table 2). Water contents in olivine are homogeneous, based on integrated absorbances obtained along a line across olivine grains (Figure 4) and our systematic analyses of core and rim of olivines, regardless of the size of the grain analyzed. Olivine water contents of Labait mantle xenoliths range from 1 to 38 ppm  $H_2O$  calculated using the absorption coefficient of Bell *et al.* [2003a]. The  $H_2O$  concentrations are 37% less if the more recent calibration of Withers *et al.* [2012] is used (Table 2). This range overlaps with that of olivine in xenoliths (6 – 33 ppm  $H_2O$  using the calibration of Bell *et al.* [2003a], 4–21 ppm using the calibration of Withers *et al.* [2012]) from the North Tanzanian Divergence of the East African Rift (Pello Hill, Eledoi within the rift, Lashaine and Olmani in the transverse volcanic belt [Baptiste *et al.*, 2015]). The concentrations calculated with the absorption coefficient of Bell *et al.* [2003a] are used henceforth and in the figures to facilitate comparison with literature data. The olivine water contents of the two age groups overlap, although two samples from the younger group record the highest olivine water contents ( $\geq 30$  ppm  $H_2O$ ; Table 2 and Figures 1e and 2b).

#### 4.2. Orthopyroxene

The O-H bands ( $2800$ – $3700\text{ cm}^{-1}$ ) of orthopyroxene polarized FTIR spectra (Figure 3b) resemble those of mantle orthopyroxene described in the literature [e.g., Skogby *et al.*, 1990; Bell *et al.*, 1995; Peslier *et al.*, 2002; Grant *et al.*, 2007a; Li *et al.*, 2008; Yang *et al.*, 2008; Xia *et al.*, 2010; Schmädicke *et al.*, 2011; Sundvall and Stalder, 2011; Peslier *et al.*, 2012; Mosenfelder and Rossman, 2013a]. Polarized spectra taken with  $E//\gamma$  have the strongest OH absorbance (Figure 3b and Table 2). Prominent bands occur at  $3600\text{ cm}^{-1}$  ( $\alpha$  and  $\beta$ ) and  $3510$ – $3580\text{ cm}^{-1}$  ( $\gamma$ ; Figure 3b). Smaller bands are sometimes present at the low wavenumbers  $3050$ – $3400\text{ cm}^{-1}$  (Figure 3b). Orthopyroxenes from Labait mantle xenoliths contain 10–150 ppm  $H_2O$  using the calibration of Bell *et al.* [1995], and the two age groups have overlapping water contents (Table 2 and Figures 1d and 2c). Orthopyroxenes in mantle xenoliths from the North Tanzanian Divergence of the East African Rift contain 97–212 ppm  $H_2O$  using the Paterson's FTIR calibration [Baptiste *et al.*, 2015]. It has been

**Table 2.** Polarized FTIR Integrated Absorbances and Water Contents for Olivine, Orthopyroxene, and Clinopyroxene of Labait Mantle Xenoliths

| Sample                          | Olivine <sup>a</sup>                  |                                       |                                       |  |  | Orthopyroxene <sup>a</sup>            |                                       |                                       |                        | Clinopyroxene <sup>a</sup>            |                                       |                                       |                           | WR <sup>b</sup><br>H <sub>2</sub> O<br>(ppm) |
|---------------------------------|---------------------------------------|---------------------------------------|---------------------------------------|--|--|---------------------------------------|---------------------------------------|---------------------------------------|------------------------|---------------------------------------|---------------------------------------|---------------------------------------|---------------------------|--|
|                                 | A <sub>x</sub><br>(cm <sup>-2</sup> ) | A <sub>β</sub><br>(cm <sup>-2</sup> ) | A <sub>γ</sub><br>(cm <sup>-2</sup> ) | H <sub>2</sub> O <sup>c</sup><br>(ppm) | H <sub>2</sub> O <sup>d</sup><br>(ppm) | A <sub>x</sub><br>(cm <sup>-2</sup> ) | A <sub>β</sub><br>(cm <sup>-2</sup> ) | A <sub>γ</sub><br>(cm <sup>-2</sup> ) | H <sub>2</sub> O (ppm) | A <sub>x</sub><br>(cm <sup>-2</sup> ) | A <sub>β</sub><br>(cm <sup>-2</sup> ) | A <sub>γ</sub><br>(cm <sup>-2</sup> ) | H <sub>2</sub> O<br>(ppm) |  |
| <i>T<sub>RD</sub> &lt; 1 Ga</i> |                                       |                                       |                                       |  |  |                                       |                                       |                                       |                        |                                       |                                       |                                       |                           |  |
| LB12                            | 4.4                                   | 14.8                                  | 28.5                                  | 9±2 (5)                                | 6±1                                    | 249.0                                 | 225.8                                 | 670.1                                 | 77±14 (2)              | 481.9                                 | 455.8                                 | 731.8                                 | 240±36 (6)                | 35   |
| LB45                            | 12.3                                  | 24.0                                  | 121.2                                 | 30±6 (5)                               | 19±4                                   | 422.2                                 | 277.5                                 | 679.9                                 | 92±13 (4)              | 256.2                                 | 192.8                                 | 336.4                                 | 111±16 (5)                | 43   |
| LB4                             | 1.4                                   | 1.3                                   | 2.5                                   | 1.0±0.4 (4)                            | 0.6±0.3                                | 229.7                                 | 242.5                                 | 329.7                                 | 54±14 (4)              | 43.6                                  | 44.2                                  | 126.8                                 | 30±8 (2)                  | 14   |
| LB50                            | 1.4                                   | 1.5                                   | 2.7                                   | 1.0±0.6 (5)                            | 0.7±0.4                                | 446.3                                 | 238.0                                 | 732.5                                 | 95±14 (4)              | 289.1                                 | 244.5 <sup>e</sup>                    | 354.0                                 | 130±72 (2)                | 23   |
| LB53                            | 1.7                                   | 1.0                                   | 32.9                                  | 7±2 (5)                                | 4.2±0.7                                | 16.5                                  | 21.1                                  | 106.2                                 | 10±3 (4)               | 27.2                                  | 25.7                                  | 61.9                                  | 16±5 (6)                  | 7  |
| KAT17                           | 12.0                                  | 24.3                                  | 168.2                                 | 39±10 (6)                              | 24±6                                   | 216.8                                 | 180.5                                 | 580.2                                 | 65±13 (4)              | 172.0                                 | 152.4                                 | 464.2                                 | 110±23 (3)                | 48   |
| <i>T<sub>RD</sub> &gt; 2 Ga</i> |                                       |                                       |                                       |  |  |                                       |                                       |                                       |                        |                                       |                                       |                                       |                           |  |
| LB24                            | 1.1                                   | 0.9                                   | 3.5                                   | 1.0±0.4 (4)                            | 0.7±0.2                                | 416.5                                 | 277.8                                 | 832.3                                 | 102±14 (5)             | 247.7                                 | 211.0 <sup>e</sup>                    | 270.8                                 | 100±62 (1)                | 20   |
| LB34                            | 1.7                                   | 3.7                                   | 43.4                                  | 9±2 (4)                                | 6±1                                    | 403.2                                 | 387.0                                 | 587.7                                 | 92±15 (5)              |                                       |                                       |                                       |                           |  |
| LB1                             | 1.4                                   | 2.4                                   | 17.7                                  | 4±1 (5)                                | 2.5±0.6                                | 116.0                                 | 101.7                                 | 406.1                                 | 42±7 (5)               |                                       |                                       |                                       |                           | 12   |
| LB9                             | 3.4                                   | 4.8                                   | 12.1                                  | 4±1 (6)                                | 2.4±0.6                                | 254.0                                 | 130.2                                 | 352.6                                 | 49±12 (5)              |                                       |                                       |                                       |                           |  |
| LB11                            | 2.6                                   | 0.6                                   | 7.6                                   | 2.0±0.6 (6)                            | 1.3±0.4                                | 616.1 <sup>e</sup>                    | 495.7                                 | 1077.7                                | 150±87 (6)             | 869.3                                 | 689.1                                 | 820.9                                 | 340±58 (2)                | 33   |
| LB14                            | 12.7                                  | 8.3                                   | 59.7                                  | 15±4 (7)                               | 10±2                                   |                                       |                                       |                                       |                        |                                       |                                       |                                       |                           |  |

<sup>a</sup>A<sub>x</sub>, A<sub>β</sub>, and A<sub>γ</sub> (cm<sup>-2</sup>), integrated absorbances beneath the O-H vibration bands with the electrical vector parallel to  $\alpha$ ,  $\beta$ , and  $\gamma$ , respectively. The calculated water contents (in ppm H<sub>2</sub>O by weight) and the corresponding standard deviations (2 $\sigma$ ) are given for each sample. Numbers in parentheses indicate the number of grains analyzed for each type of mineral.

<sup>b</sup>Whole-rock (WR) water contents were reconstructed from measured water contents in minerals and estimated mineral modes (Table 1) [Lee and Rudnick, 1999]. No WR contents are provided where H<sub>2</sub>O data for clinopyroxene are missing. Garnets are generally broken down to kelyphite and are assumed to have a negligible contribution to the WR water because of their low water content. The WR water contents are the same if we assume all garnets in xenoliths have 1 ppm H<sub>2</sub>O as detected in LB24 garnet, which is the only garnet could be analyzed for water.

<sup>c</sup>Olivine water contents calculated with the absorption coefficient of Bell *et al.* [2003].

<sup>d</sup>Olivine water contents calculated with the absorption coefficient of Withers *et al.* [2012].

<sup>e</sup>A<sub>x</sub> or A<sub>β</sub> in italic was calculated based on the A<sub>x</sub>/A<sub>β</sub> from other samples because a grain oriented  $\alpha$  or  $\beta$  was not present in the mineral mount. Therefore, the water contents of these three samples (LB11 orthopyroxene, LB24 clinopyroxene, and LB50 clinopyroxene) may be inaccurate shown by their large uncertainties.

shown that the Paterson's method underestimates water concentration [Rossman, 2006] but there is no systematic relationship with the orthopyroxene specific calibration of Bell *et al.* [1995]. Therefore, Labait orthopyroxenes may have less water than those from the North Tanzanian Divergence.

Most incompatible trace element contents in orthopyroxene are lower than those of the primitive mantle (Figure 5a–5d and supporting information Table S1) [McDonough and Sun, 1995]. Primitive mantle normalized REE patterns of orthopyroxenes are typically flat to slightly light REE depleted (Figure 5a–5d), while Ti, Nb, and Ta show positive anomalies compared to the REE except for Ti in LB9 (Figure 5a–5d). The range of trace element abundances in orthopyroxene overlaps among the four different lithologies and between the two different age groups (Table 1 and Figure 5a–5d).

#### 4.3. Clinopyroxene

Polarized FTIR spectra of clinopyroxene from Labait mantle xenoliths are similar to those from other locations [e.g., Skogby *et al.*, 1990; Bell *et al.*, 1995; Peslier *et al.*, 2002; Grant *et al.*, 2007a; Li *et al.*, 2008; Yang *et al.*, 2008; Xia *et al.*, 2010; Sundvall and Stalder, 2011; Peslier *et al.*, 2012; Mosenfelder and Rossman, 2013b]. The E// $\gamma$  spectra have the main OH bands at 3450 cm<sup>-1</sup> (e.g., LB12) or 3520 cm<sup>-1</sup> (e.g., LB45), or the two main bands can have roughly equal heights (e.g., LB11). The main OH bands of the E// $\alpha$  and  $\beta$  spectra are located between wavenumbers 3440 cm<sup>-1</sup> and 3640 cm<sup>-1</sup> (Figure 3c). The water content of clinopyroxene in Labait xenoliths varies from 16 to 340 ppm H<sub>2</sub>O (Table 2 and Figures 1c and 2d). Of the two samples from the older group that contained clinopyroxene that could be analyzed for water, one has similar clinopyroxene water content to the clinopyroxene in the younger group, while the other records the highest value (340 ppm H<sub>2</sub>O in LB11; Table 2 and Figure 1c).

Incompatible trace element concentrations of clinopyroxene are generally higher than those of orthopyroxene in the Labait mantle xenoliths. All clinopyroxenes record a systematic enrichment from heavy to light REE (LREE are 2–10 times primitive mantle values, with the highest concentrations at Nd, Pr, or Ce; Figure 5e and 5f and supporting information Table S2). The clinopyroxenes from the younger group have slightly higher LREE contents than those from the older group. High field strength elements and Y are depleted compared to elements with similar compatibility (Figure 5g and 5h), likely reflecting subsolidus partitioning with orthopyroxene [e.g., Rampone *et al.*, 1991; McDonough *et al.*, 1992].

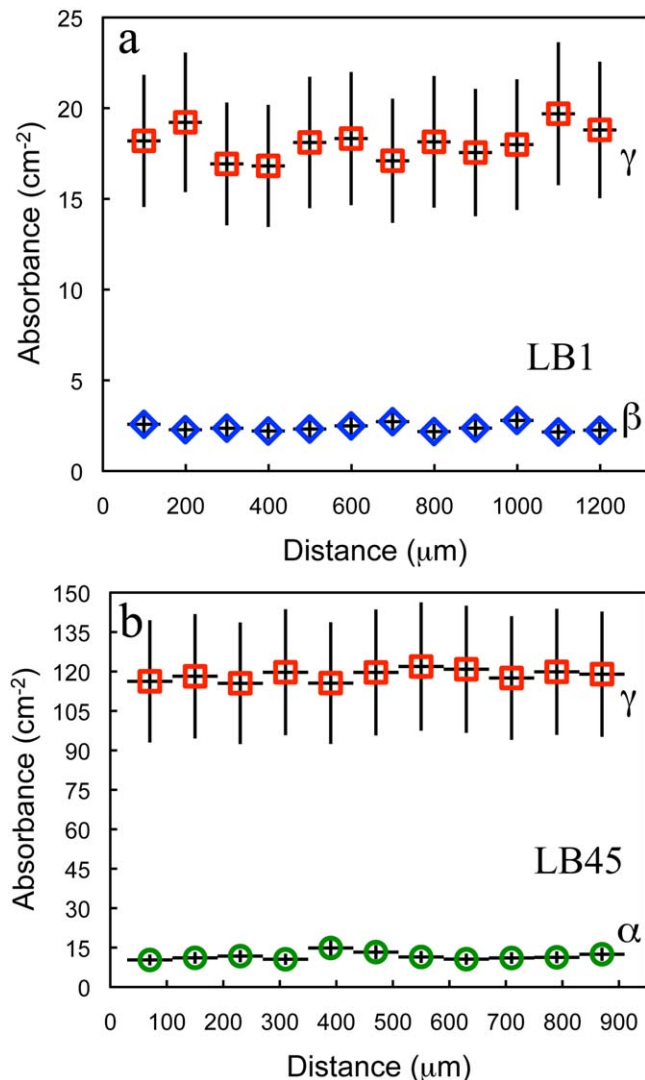


**Figure 4.** Integrated polarized infrared absorbance of the OH bands across olivine grains from edge to edge for two samples: (a) LB1 (olivine 28), (b) LB45 (olivine 63). Analyses were made with an aperture of 80 μm (error bar for distance), with the uncertainty on the absorbance for the olivine being 20% (2 $\sigma$ ). The essentially flat profiles of water across the olivine grains are interpreted to indicate minimal diffusional loss or gain of olivine H during xenolith transport by the host magma.

and supporting information Table S3). Generally, LB24 garnets are slightly middle and heavy REE (MREE and HREE) that are close to those of primitive mantle. Fresh garnet contains less large-ion lithophile elements relative to kelyphite (Figure 6d), though both have the same major element compositions [Lee and Rudnick, 1999].

## 5. Discussion

### 5.1. Water Diffusion in Garnet and Rapid Magma Ascent

Kelyphite, which is widespread in Labait mantle xenoliths [Lee and Rudnick, 1999; Koornneef et al., 2009], is the product of decompression breakdown of garnet [e.g., Reid and Dawson, 1972; Messiga and Bettini, 1990; Lee and Rudnick, 1999; Godard and Martin, 2000; Dégi et al., 2010], requiring decompression from the deep crust to the surface lasting more than a year [Dégi et al., 2010]. This analysis, however, does not distinguish between the two episodes of garnet breakdown seen in the Labait peridotites: creation of relatively coarse symplectite and formation of very fine-grained kelyphite [Lee and Rudnick, 1999]. Furthermore, the duration

### 4.4. Garnet

Garnets in Labait mantle xenoliths are typically decomposed into kelyphite (Figure 6a) [Chesley et al., 1999; Lee and Rudnick, 1999; Koornneef et al., 2009]. Only garnets from sample LB24 had pristine cores that could be analyzed. The IR spectra in the region of 3700–3400 cm<sup>-1</sup> (Figure 6b) are consistent with the absorption patterns attributed to H structurally bound to O in garnet [e.g., Bell and Rossman, 1992b; Bell et al., 1995; Matsyuk et al., 1998; Peslier et al., 2012]. Water is heterogeneously distributed in two out of six garnet grains analyzed, with enrichment at the boundary with kelyphite, as shown by the variation in size of the OH band at 3625–3700 cm<sup>-1</sup> (Figure 6b). The cores of these garnets have relatively low water content of ~1 ppm H<sub>2</sub>O (Figure 6b), as do the other garnets that are homogeneous in terms of water content in this sample. Large OH bands in the spectrum of kelyphite indicate that it may contain significant amounts of water (Figure 6c), which is consistent with water enrichment in garnet toward the kelyphite (Figure 6b and 6c).

In contrast to water contents, incompatible trace element concentrations are homogeneous within LB24 garnets (Figure 6d)

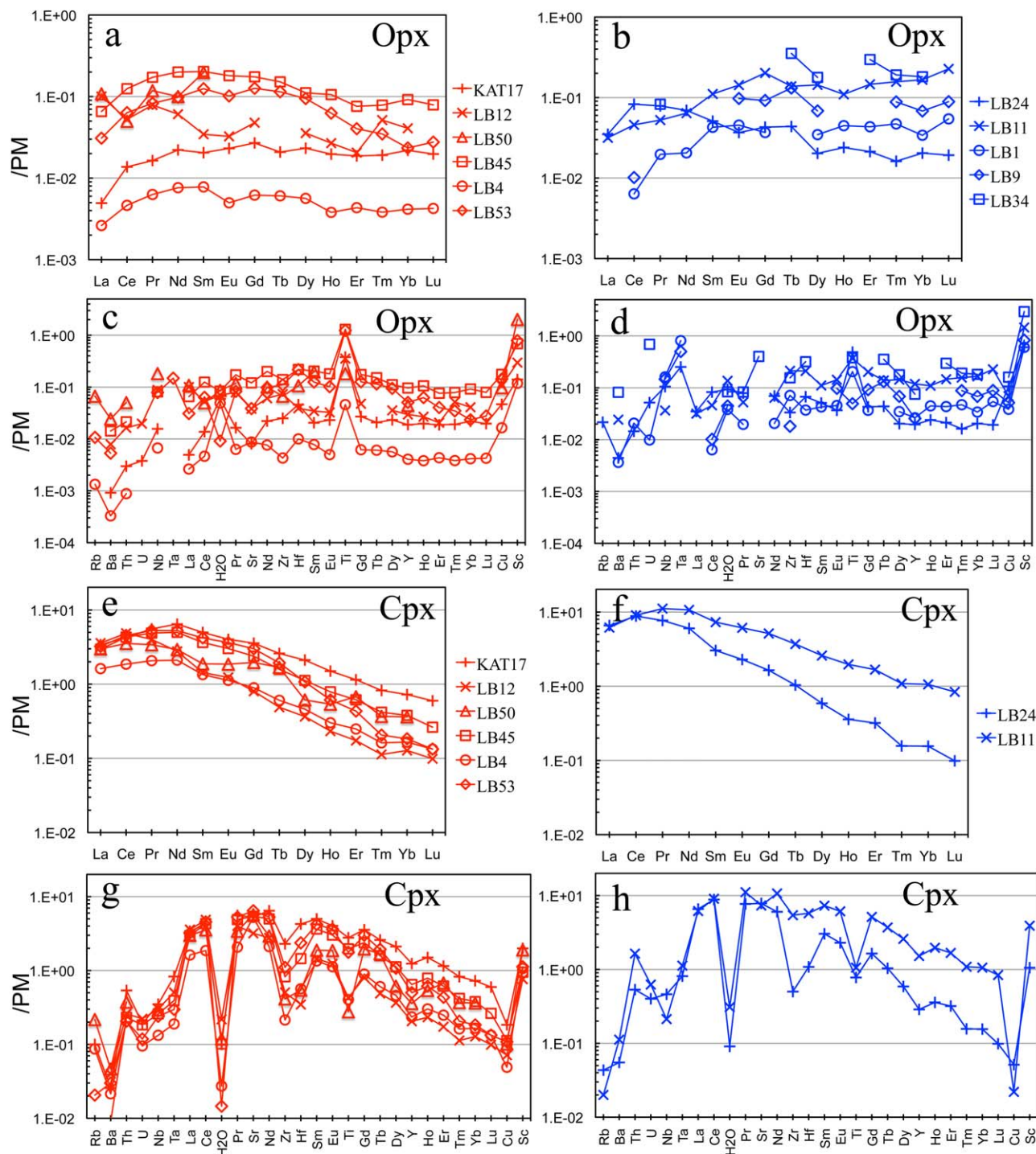


**Figure 5.** Primitive mantle (PM) normalized trace element diagrams and rare earth element distribution patterns of orthopyroxene and clinopyroxene in Labait mantle xenoliths. Primitive mantle values from McDonough and Sun [1995], except that for water [Palme and O'Neill, 2007]. (a, c, e, and g) Red lines and symbols identify the deeper, <1 Ga xenoliths, while (b, d, f, and h) blue ones are for the shallower, >2 Ga samples.

of garnet breakdown calculated by Dégi *et al.* [2010] does not likely represent the time scale of magma ascent, which must be on the order of hours based on Stokes settling velocities of entrained peridotite xenoliths [Spera, 1980].

The presence of water in the host magma can significantly facilitate kelyphite formation [e.g., Messiga and Bettini, 1990; Godard and Martin, 2000]. Enrichments in water (our FTIR measurements, Figure 6c) and in

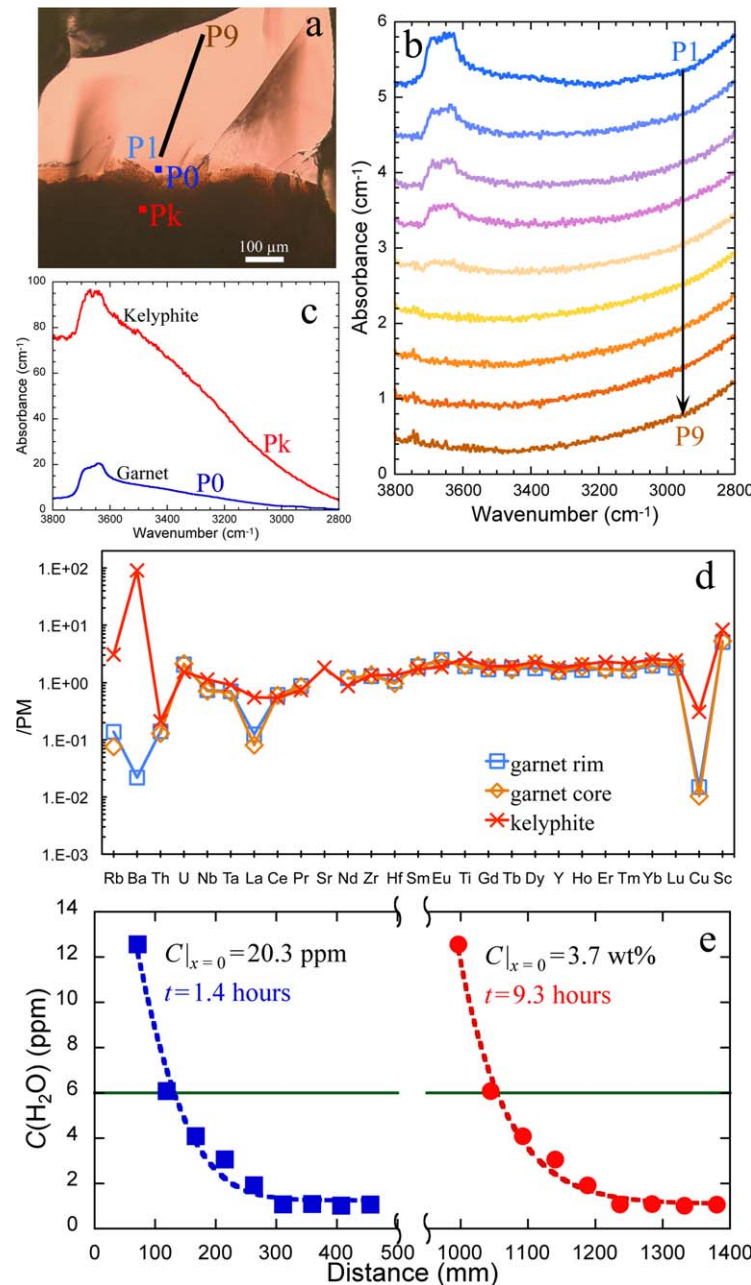


**Figure 6.** (a) Plane polarized light photomicrograph of one LB24 garnet grain. Note that the garnet is enclosed by kelyphite (dark area in the bottom part of the picture). Texture difference between the edge (P0) and core (P1–P9) of garnet based on optical observation (Figure 6a) indicates that the edge (P0) has been altered. (b) Unpolarized FTIR absorption spectra for garnet in O–H bond region show H variation from rim (P1) to core (P9) corresponding to positions shown by the black line in Figure 6a. (c) Unpolarized FTIR spectra from the edge of garnet and kelyphite corresponding to locations P0 and Pk in Figure 6a, respectively. Water contents at P0 and Pk are significantly higher than inside the garnet, which is zoned with higher water content at the edge (P1) compared to its core (P9). Grain thickness for all spectra is normalized to 1 cm. (d) Primitive mantle (PM) normalized [McDonough and Sun, 1995] trace element diagrams of LB24 garnet (core and rim) and kelyphite. (e) Water content profile across a LB24 garnet grain (Figure 6a) and modeling with two different boundaries: outer kelyphite rim (red solid circle) and inner kelyphite rim (blue solid square). Curves indicate a fit of water diffusion profile (see text for discussion). The garnet water content at the diffusion boundary (the inner kelyphite rim) inferred from the diffusion profile (blue dashed line) is 20.3 ppm (a fitting parameter), indicating a relatively dry host magma ( $\sim 0.6$  wt.% H<sub>2</sub>O). The water content at the outer kelyphite boundary inferred from the diffusion profile (red dashed line) is 3.7 wt.% (a fitting parameter), exceeding the maximum experimentally determined water solubility in garnets ( $\sim 0.1$  wt.%) [Mookherjee and Karato, 2010], indicating that diffusion occurred much later than the onset of kelyphite formation. Green solid horizontal line shows the calculated water content of garnet in equilibrium with LB24 olivine in terms of water ( $D^{\text{ol/melt}} = 0.0006$  and  $D^{\text{grt/melt}} = 0.0033$  [Tenner et al., 2009]).

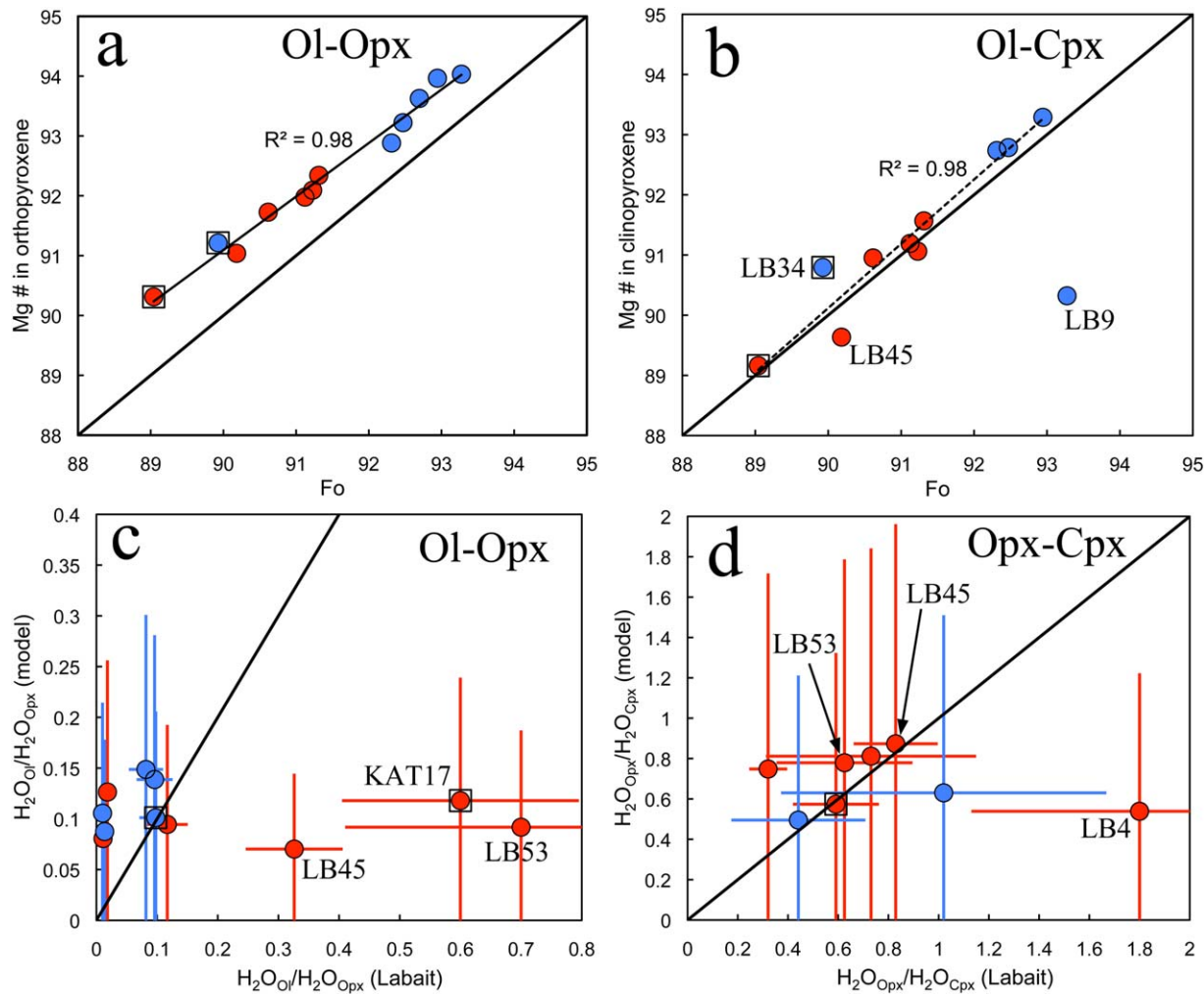


**Figure 7.** Forsterite content of olivine versus Mg # ( $(Mg/(Mg+Fe)) \times 100$ ) of (a) coexisting orthopyroxene and (b) clinopyroxene in Labait mantle xenolith. Orthopyroxenes exhibit a tight correlation, whereas clinopyroxenes are more scattered. Comparison of water distributions (c) between olivine and orthopyroxene, and (d) between pyroxenes in Labait mantle xenoliths with the partition coefficients calculated from experimental data (model) [Tenner et al., 2009; O'Leary et al., 2010]. Solid lines represent 1:1 correspondence. Error bars represent  $2\sigma$  standard uncertainty calculated from the error propagation of uncertainties on the partition coefficients and measured water contents. Note that due to the experimental difficulties, the uncertainties of partition coefficients typically are much larger than those of water ratios between Labait mantle minerals.

soluble large ion lithophile elements (LILE, e.g., Rb and Ba in Figure 6d) and Na [Lee and Rudnick, 1999] in kelyphite relative to garnet are consistent with a water-facilitated reaction. Water zonation seen in garnet (Figure 6b) but not in olivine or pyroxene suggests kelyphite formation played an essential role in the diffusion of water into the garnet, which must have happened during the entrainment of the xenolith in the host magma. The water-rich kelyphite (Figure 6c) may have served as the source of water that diffused into the garnet. Therefore, initiation of water diffusion into LB24 garnet may have occurred only after the onset of kelyphite formation. Conversely, the kelyphite rim likely grows at the expense of garnet during magma ascent. This kelyphitization process thus could also have erased part of the water diffusion profile in the garnet. Nevertheless, the zoned water content in LB24 garnets (Figure 6b) can be used to place constraints on magma ascent rates.

Using experimentally determined H diffusion coefficients in garnet [e.g., Wang et al., 1996; Blanchard and Ingrin, 2004; Kurka et al., 2005; Ingrin and Blanchard, 2006; Farver, 2010], we estimate the time required to produce the observed water profile via diffusion. The diffusion interface between kelyphite (or hydrous magma) and garnet could be anywhere from the outer (red solid curve) to inner boundary (blue dotted curve) of the 900 micron-thick kelyphite (Figure 6e). The calculation is simplified as diffusion through a semi-infinite media (i.e., garnet) with constant initial and surface water contents as fitting parameters

(Figure 6e) [e.g., Zhang, 2010]. The effects of temperature, pressure or compositional variation on H diffusivity of garnet are not considered, i.e., a constant diffusivity of  $1.1 \mu\text{m}^2/\text{s}$  is calculated at  $1100^\circ\text{C}$  and an oxygen fugacity  $f_{\text{O}_2} = 10^{-16}$  atm [Blanchard and Ingrin, 2004]. The zoned water content in garnet can be modeled by diffusion of H from the kelyphite to the core of the garnet in a few hours (Figure 6e). If the water content profile was created during ascent of the xenolith from a depth of  $\sim 140$  km, which is the equilibration depth of sample LB24 (Table 1) and is assumed to be the depth of onset of kelyphite formation, the host magma ascent rate ranges from 4 to 28 m/s with respect to that of the diffusion interface. This range is similar to that estimated for the olivine-melilititic magmas (8.5 – 36.0 m/s) in the Lake Natron-Engaruka monogenetic volcanic field based on crack propagation [Mattsson, 2012]. The inferred ascent rate of Labait magma is close to that estimated for the Pali-Aike alkali olivine basalts ( $6 \pm 3$  m/s) [Demouchy et al., 2006], and kimberlitic magmas, in general ( $> 4$  m/s) [e.g., Sparks et al., 2006; Peslier et al., 2008], but is an order of magnitude faster than that of Mexican mafic-alkalic magmas (0.2–0.5 m/s) [Peslier and Luhr, 2006] and Hawaiian nephelinites (0.2–25.3 m/s) [Peslier et al., 2015].

### 5.2. Preservation of Mantle Water Contents

Labait mantle xenoliths can potentially be used to determine the water content of the Tanzanian cratonic mantle lithosphere if the water contents are preserved in NAMs after the peridotites were entrained as xenoliths in the host magma. Chemical compositions of mantle xenoliths can potentially be altered during both magma ascent and postemplacement weathering [e.g., Miller et al., 1987; Li et al., 2008].

Although the xenoliths have been exposed to weathering since the Late Pleistocene when the Labait olivine-melilititic magma erupted [Rudnick et al., 1999], they are embedded in lava and tuff, appear to be serpentine-free and are generally fresh [Chesley et al., 1999; Lee and Rudnick, 1999]. Individual mineral grains were hand picked for this study and examined using a petrographic microscope to be optically clear. Furthermore, no IR bands for alteration products (serpentine, amphibole) were observed in our spectra (Figure 3).

Exchange of chemical components between NAMs in mantle peridotites and the host magma may occur at elevated temperatures during transport to the surface. However, as the water content in Labait olivines is below the saturation level at mantle conditions [Zhao et al., 2004; Mosenfelder et al., 2006], degassing is unlikely to have occurred before the ascent of the host magma. During entrainment in the host magma, water in NAMs from mantle xenoliths may be partly lost if the magma ascends slowly enough to allow water to diffuse out of mantle minerals and the saturation point is reached due to decreasing water fugacity [Mosenfelder et al., 2006]. Such a degassing process has been inferred from water diffusion profiles preserved in olivine from mantle xenoliths [e.g., Demouchy et al., 2006; Peslier and Luhr, 2006; Li et al., 2008; Peslier et al., 2008, 2010]. Our FTIR data show that water is homogeneously distributed within the Labait olivines (Figure 4) and pyroxenes. Moreover, water in eight olivines out of 11 appears to be in equilibrium with coexisting orthopyroxenes (see section 5.3, Figure 7c), which further suggests little to no H loss. Only two garnets from sample LB24 show water diffusion profiles that can be interpreted as resulting from infiltration of water from kelyphite during xenolith transport (Figure 6). The lack of water zonation in Labait olivine and pyroxene may be due to a combination of the following two factors: (1) a hydrous host magma in which water fugacity was high enough to prevent degassing of mantle minerals, i.e., water in olivine was undersaturated with respect to the host [e.g., Mosenfelder et al., 2006], and (2) entrainment time in the host magma was likely short, and its ascent may have been too fast to allow for significant H diffusion through the xenolith minerals. The first hypothesis is consistent with the evidence for water incorporation in secondary kelyphite that formed during xenolith entrainment and ascent; the second hypothesis is consistent with the rapid ascent rates calculated from modeling the water profiles in LB24 garnet. We therefore conclude that the water contents of olivine and pyroxene measured here represent mantle values.

### 5.3. Inter-mineral equilibration of water

Labait forsterite contents (Fo) correlate with Mg# of coexisting orthopyroxenes ( $r^2 = 0.98$ , Figure 7a) [Lee and Rudnick, 1999], which is consistent with an equilibrium assemblage. Three samples (LB9, LB34, and LB45), however, lie off the correlation between Fo and clinopyroxene Mg# ( $r^2 = 0.98$ , Figure 7b), indicating that their clinopyroxene is not in equilibrium with olivine and orthopyroxene. Clinopyroxene is likely secondary or altered (Figure 7b), given that it occurs in a metasomatic vein (LB9) and as zoned crystals (LB45), and xenolith LB34 is enriched in Fe [Lee and Rudnick, 1999].

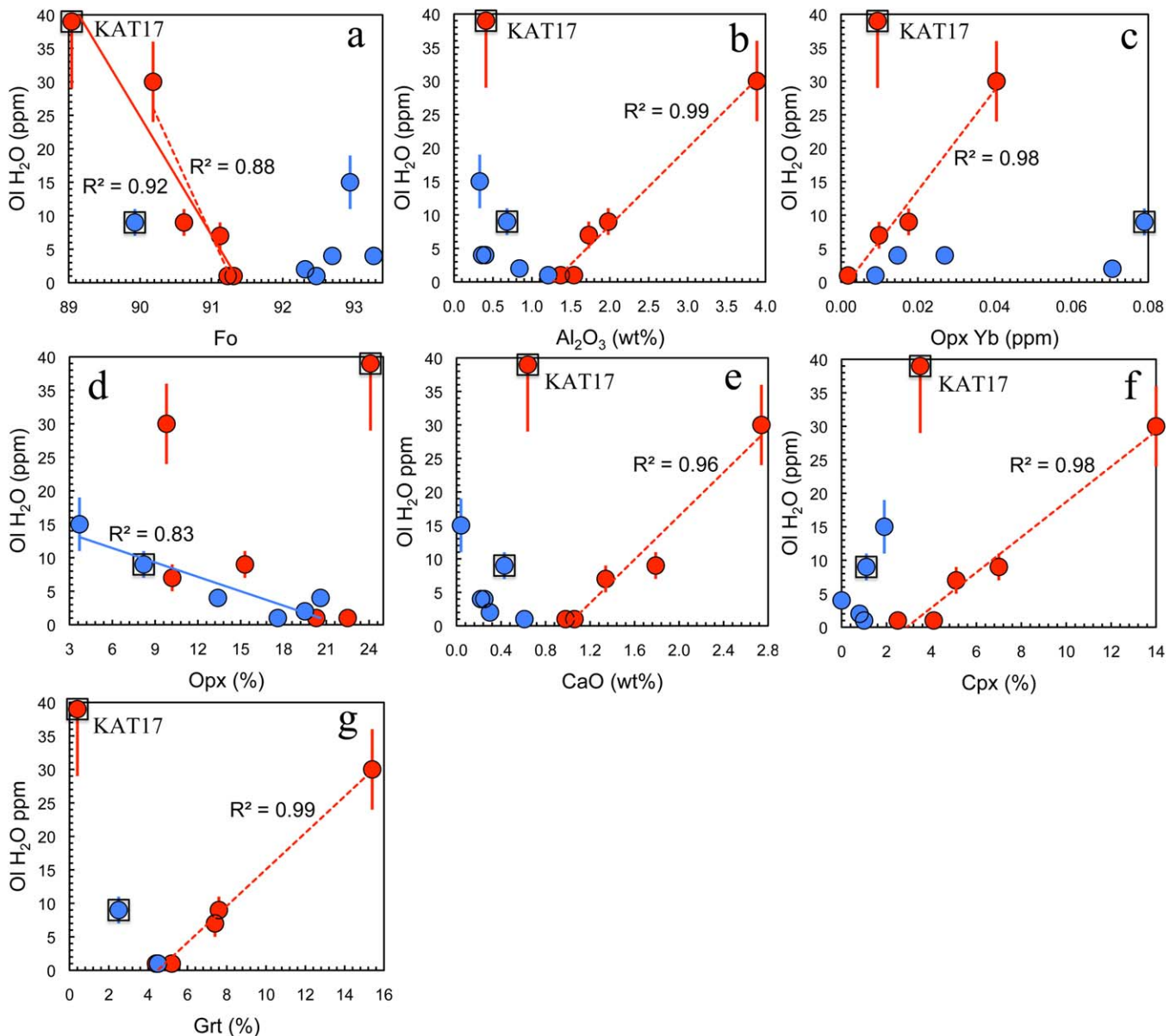


**Figure 8.** Olivine (Ol) water content (ppm H<sub>2</sub>O) versus (a) forsterite content, (b) whole-rock Al<sub>2</sub>O<sub>3</sub> content (wt.%), (c) orthopyroxene Yb content (ppm), (d) modal percentage of orthopyroxene, (e) whole-rock CaO content (wt.%), (f) modal percentage of clinopyroxene, and (g) modal percentage of garnet. The major-element data and mineral modal abundance are from Lee and Rudnick [1999]. Error bars represent the 2 $\sigma$  uncertainty. The lines are linear regression, which show the correlation between olivine water content and other chemistry. The dashed lines represent the linear regression of the data excluding the data point labeled in this group (i.e., KAT17 in the specific figures).

Experimentally determined partition coefficients for water between NAMs can be compared to those measured in the Labait xenoliths to assess inter-mineral equilibration (Figure 7c and 7d). Partition coefficients of water between olivine and basaltic melt published in the literature [e.g., Aubaud *et al.*, 2004; Hauri *et al.*, 2006; Kohn and Grant, 2006; Tenner *et al.*, 2009; Novella *et al.*, 2014] exhibit major discrepancies. In the absence of a good understanding of the effects of temperature, pressure and chemical components on water partitioning between olivine and melt, a constant value of 0.0006 [Tenner *et al.*, 2009] is used here. Partitioning of water between pyroxene and basaltic melt depends on the Al and Ca contents in pyroxene [Aubaud *et al.*, 2004; Hauri *et al.*, 2006; Keppler and Bolfan-Casanova, 2006; Grant *et al.*, 2007b; Aubaud *et al.*, 2008; Tenner *et al.*, 2009; O'Leary *et al.*, 2010; Novella *et al.*, 2014]. In addition, water partitioning between clinopyroxene and basaltic melt is temperature-dependent [O'Leary *et al.*, 2010]. The partition coefficients between pyroxene and basaltic melt were calculated using Equations 11 (for clinopyroxene) and 12 (for orthopyroxene) in O'Leary *et al.* [2010] at the equilibration temperature calculated using major-element

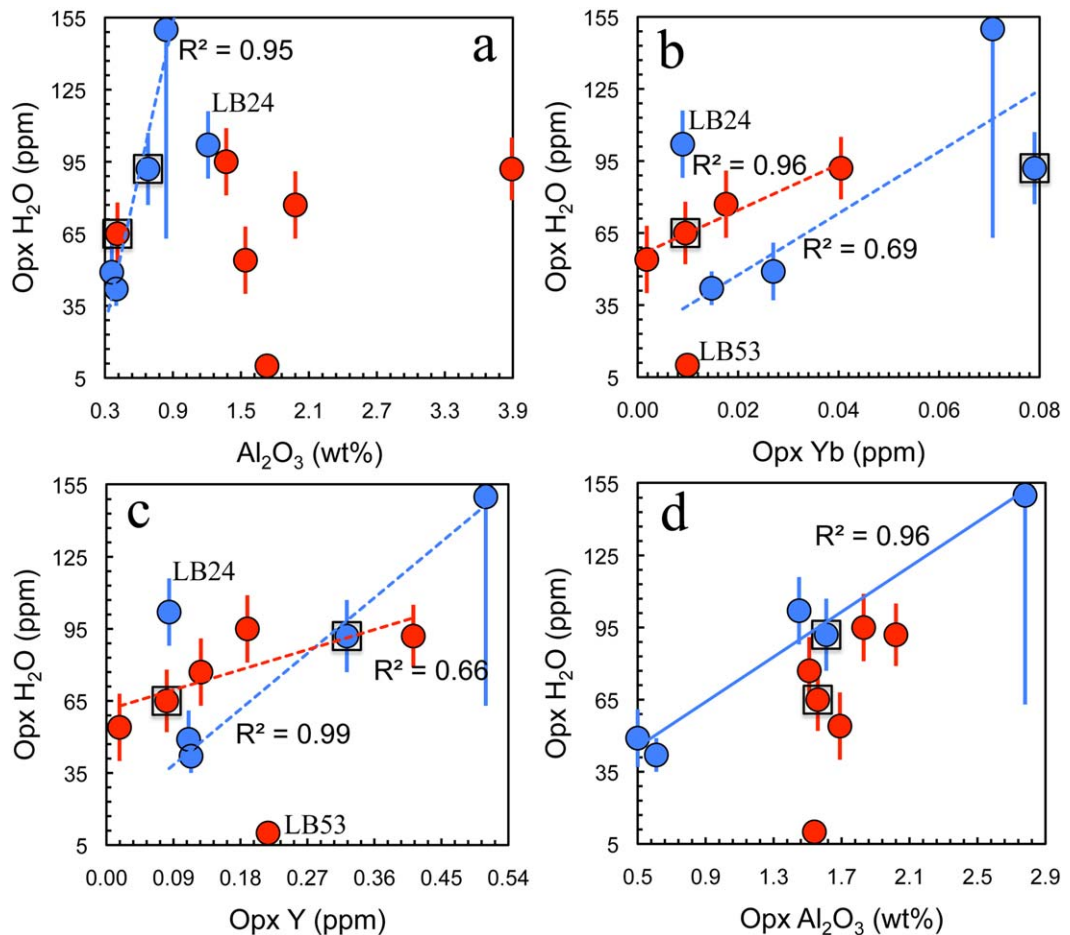


**Figure 9.** Orthopyroxene (Opx) water content (ppm H<sub>2</sub>O) versus, (a) whole-rock Al<sub>2</sub>O<sub>3</sub> content (wt.%), (b) orthopyroxene Yb content (ppm), (c) orthopyroxene Y content (ppm), and (d) orthopyroxene Al<sub>2</sub>O<sub>3</sub> content (wt.%). The major-element data are from Lee and Rudnick [1999]. Error bars represent the 2 $\sigma$  uncertainty. The lines are linear regressions, which show the correlation between orthopyroxene water content and other chemistry. The dashed lines represent the linear regression of the data excluding the data point labeled in the group (i.e., LB24 and LB53 in the specific figures).

geothermometers (Table 1). The distribution of water between Labait olivine and orthopyroxene in xenoliths LB45, LB53, and KAT17, all of which are from the younger group, deviates from equilibrium (Figure 7c). The disequilibrium may result from recent metasomatic hydration of olivine, with insufficient time for re-equilibration. By contrast, the water distribution between orthopyroxene and clinopyroxene indicate that most Labait pyroxenes may be in equilibrium for water except for the young xenolith LB4 (Figure 7d). Water disequilibrium between phases in the younger group of peridotites may reflect heterogeneous metasomatism in terms of time (multiple metasomatic events), composition (not necessarily water-rich) and space (distance of the peridotite from metasomatic conduit). Irrespective of whether water is in equilibrium between olivines and pyroxenes in Labait xenoliths, our measurements fall within the range of literature values of mantle minerals from other cratons (Figure 2).

#### 5.4. Effects of Melting and Metasomatism on Water Contents

##### 5.4.1. The >2 Ga Peridotites

The >2 Ga Labait peridotites are residues of 30–50% partial melting (Figure 1a) [Lee and Rudnick, 1999]. The LREE enriched clinopyroxenes in these samples (Figure 5f) and the high-Fe content of sample LB34 [Lee and Rudnick, 1999] are indicative of interaction with Fe and LREE-rich melts. The water contents measured here are also consistent with recent overprinting.

Olivine water contents do not show any relationship to indices of melting (Fo, whole-rock Al<sub>2</sub>O<sub>3</sub>, or orthopyroxene HREE; Figure 8a–8c). The only exception is a decrease with increasing amount of orthopyroxene in the peridotite (Figure 8d), which can result from partial melting [Walter, 1998].

Correlations between orthopyroxene water content and indices of melting are present if sample LB24 is excluded (dashed lines; Figure 9a–9c). LB24 equilibrated at >4 GPa while all other peridotites from the >2 Ga group are from shallower depths ( $\leq 3.2$  GPa; Table 1), which could account for its different conditions of hydration. Moreover, orthopyroxene water and  $\text{Al}_2\text{O}_3$  contents correlate positively for all >2 Ga samples ( $r^2 = 0.96$ , Figure 9d), consistent with the increased H partition coefficient and solubility in orthopyroxene with increasing Al content [e.g., *Keppler and Bolfan-Casanova*, 2006; *Tenner et al.*, 2009; *O'Leary et al.*, 2010; *Novella et al.*, 2014].

Only two clinopyroxenes from the older group (LB24 and LB11) have been analyzed for water and trace elements and there is consequently not enough data to infer any relationship. LB11 clinopyroxenes have higher water and incompatible trace element contents compared to those of the younger group, consistent with water addition from a hydrous REE-bearing melt (Figure 5f and 5h). The Na content of clinopyroxene, measured by electron microprobe [*Lee and Rudnick*, 1999], can also be a good tracer of metasomatism [cf. *Ionov et al.*, 2006; *O'Reilly and Griffin*, 2013], but no correlation is observed with water contents of olivine or orthopyroxene in the >2 Ga group.

Finally, the water contents of olivine and orthopyroxene of the Fe-rich sample LB34 are not the highest amongst the >2 Ga group, indicating that water and Fe contents in these minerals are not correlated. All these observations suggest that the metasomatic history of the peridotites probably involved several events following initial melting >2 Ga ago, erasing any simple trend, as also seen in their Sr-Nd systematics [*Aulbach et al.*, 2011]. Overall, the observations are qualitatively consistent with only the orthopyroxene having retained some of the signature of partial melting in its water and trace element contents.

In order to quantitatively test the above hypothesis, simple equilibrium and fractional melting models [*Shaw*, 1979; *Norman*, 1998] were carried out (Figure 1b–1d). The calculated whole-rock water content of most >2 Ga peridotites falls within the range of equilibrium and fractional melting curves of a primitive mantle (PM) source (assuming the highest PM water content found in the literature, 1100 ppm  $\text{H}_2\text{O}$  of *Palme and O'Neill* 2007) (Figure 1b). The pyroxenes and three out of five olivines, however, have water contents too high to be simply explained by partial melting of the depleted mantle (DM) or PM (the orange and red curves in Figure 1c–1e, respectively). Fitting the melting curves through the data would require increasing either the initial mantle water content to unreasonable amounts (higher than that of PM) or the mineral/melt partition coefficient of H to values unmatched by any experimental data [*Hirschmann et al.*, 2009; *Tenner et al.*, 2009; *O'Leary et al.*, 2010; *Novella et al.*, 2014]. Thus, a process other than melt depletion is required to explain the range of water contents of the >2 Ga Labait peridotites.

One possibility is that the melts that introduced additional Fe and LREE to some of the Labait peridotites also introduced water. This scenario can be modeled by a melt-rock interaction process [*DePaolo*, 1981], whereby variously depleted peridotites are infiltrated by water-bearing melts (blue dashed curves in Figure 1b–1e). The range of water contents of the Labait >2 Ga peridotites can be reproduced, including those of the pyroxenes and olivine, with <1 wt.% addition of a relatively dry melt (0.5 wt.%  $\text{H}_2\text{O}$ ; Figure 1b–1e).

#### 5.4.2. The <1 Ga Peridotites

The younger Labait peridotites (excluding Fe-rich sample KAT17) could represent simple residues of 5–30% partial melting of a lherzolite (Figure 1a). However, the inferred pressures of melting (<4 GPa, Figure 1a) are lower than the equilibration pressures of these peridotites ( $\geq 4$  GPa; Table 1 and Figure 2). The lower pressure melting curves correspond to higher Fe contents (Figure 1a) [*Herzberg*, 2004]. The discrepancy between inferred melting pressure and equilibration pressures could be explained by metasomatic addition of Fe to these deep-seated samples. The high proportion of Fe-rich dunites in the Labait xenolith suite is evidence for the passage of Fe-rich melts [*Lee and Rudnick*, 1999], as are the Fe-enrichments observed in some samples (e.g., KAT17).

Water content of olivines in the younger mantle peridotites is negatively correlated with forsterite content (Figure 8a) and, excluding the Fe-rich sample KAT17, positively correlated with whole-rock  $\text{Al}_2\text{O}_3$  (Figure 8b), orthopyroxene HREE contents (Figure 8c) and whole-rock CaO contents (Figure 8e), modal abundances of clinopyroxene (Figure 8f), and garnet (Figure 8g) in the peridotite. These trends are consistent with either partial melting or refertilization processes. In particular, the correlation with forsterite contents (Figure 8a) is consistent with the experimentally determined relationship between water solubility in olivine and forsterite content [e.g., *Zhao et al.*, 2004; *Keppler and Bolfan-Casanova*, 2006]. Furthermore, neither olivine nor

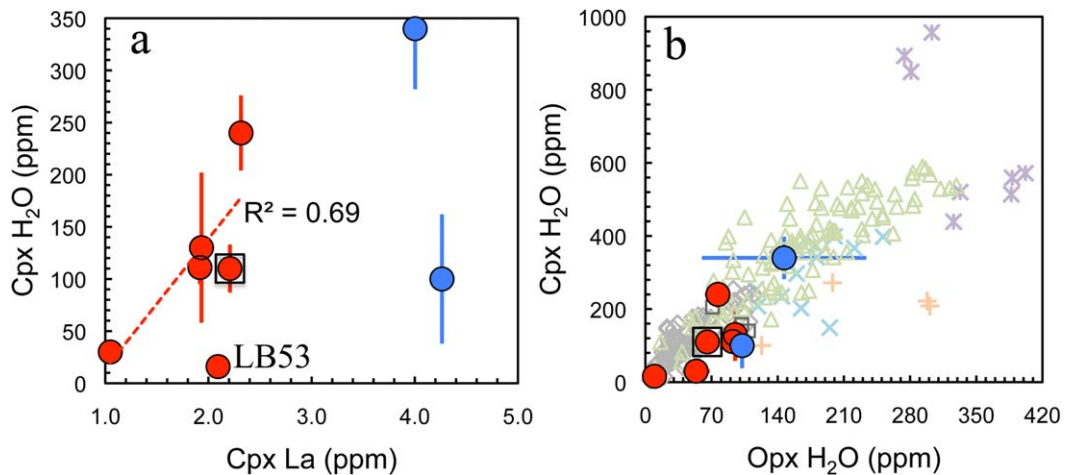


**Figure 10.** Clinopyroxene (Cpx) water content (ppm H<sub>2</sub>O) versus (a) clinopyroxene La content (ppm), and (b) orthopyroxene water content (ppm H<sub>2</sub>O). Error bars represent the 2 $\sigma$  standard uncertainty. The dashed lines represent the linear regressions of the data excluding LB53 as labeled. Literature pyroxene water data in Figure 10b are those from Archean cratons: Kaapvaal [Grant et al., 2007a; Sundvall and Stalder, 2011; Peslier et al., 2012] and Siberian [Doucet et al., 2014], Colorado plateau that shows subduction related water enrichments [Li et al., 2008] and modified cratons such as North China craton that lost its mantle root (open diamond) [Yang et al., 2008; Bonadiman et al., 2009; Xia et al., 2010, 2013], and off craton xenolith locations from continental margins in Namibia, Southwest USA, West Canada, Mexico, Antarctica, Southeast China (open triangle) [Bell and Rossman, 1992a; Peslier et al., 2002; Grant et al., 2007a; Li et al., 2008; Bonadiman et al., 2009; Yu et al., 2011; Hao et al., 2014], and mantle wedge setting—Simcoe (open square [Peslier et al., 2002]).

orthopyroxene water contents are related to clinopyroxene LREE enrichment, which also characterizes metasomatism in these rocks.

Orthopyroxene water contents, on the other hand, do not correlate with any of the indices of melting, with the exception of orthopyroxene Yb content, if water-poor LB53 is excluded (Figure 9b). Excluding again sample LB53, orthopyroxene water contents correlate positively with pressure of equilibration (Figure 2c) consistent with partial melting. The lack of correlation between orthopyroxene water and Al<sub>2</sub>O<sub>3</sub> contents, which would be expected from partitioning and solubility properties of water in orthopyroxene [Aubaud et al., 2004; Hauri et al., 2006; Keppler and Bolfan-Casanova, 2006; Grant et al., 2007b; Aubaud et al., 2008; Tanner et al., 2009; O’Leary et al., 2010; Novella et al., 2014], may be related to the narrow range of orthopyroxene Al<sub>2</sub>O<sub>3</sub> contents in the younger peridotites (1.5–2 wt.% [Lee and Rudnick, 1999]) (Figure 9d).

The water contents of the Labait clinopyroxenes also do not correlate with any melting indices. Instead, clinopyroxene water content increases with increasing LREE content (excluding LB53), consistent with metasomatism by water and LREE bearing melts (Figure 10a). In summary, water contents of the younger group of Labait peridotites may have been controlled by plume-related metasomatism.

The water contents of the younger peridotites can be compared to simple melting curves as described above (Figure 1b–1e). Like the older group, the whole-rock water contents of the younger peridotites appear consistent with the melting curves of a PM source (Figure 1b). However, the pyroxene water contents, as well as those of some olivines, are too high to be simply explained by partial melting (Figure 1c–1e), and are consistent with their water contents being enhanced by interaction with relatively dry (<1 wt.% H<sub>2</sub>O) LREE-enriched melts (Figure 1d and 1e).

### 5.5. Craton-Plume Interaction beneath Labait

The Labait peridotites record abundant petrologic, compositional and isotopic evidence for interaction with melts derived from the plume responsible for the East African Rift [Chesley et al., 1999; Lee and Rudnick, 1999; Rudnick et al., 1999; Aulbach et al., 2008, 2011], yet they, and other mantle xenoliths from Northern Tanzania [Baptiste et al., 2015], have relatively low water contents compared to other cratonic peridotites (Kaapvaal and Siberian) and peridotites from other locations around the world (Figures 2b–2d and 10b). Although the Re depletion age separates the samples into two groups, a shallow Archean cratonic lithosphere underlain by a younger (<1 Ga) more fertile mantle lithosphere [Chesley et al., 1999], all peridotites record interaction with the same type of melts, as seen by the similarity of trace element patterns of

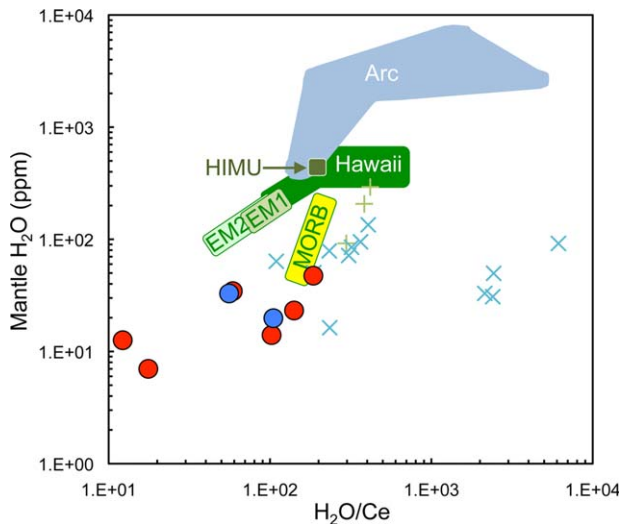


**Figure 11.**  $\text{H}_2\text{O}/\text{Ce}$  ratios versus water contents of cratonic peridotites (symbols as in Figure 2) compared to  $\text{H}_2\text{O}/\text{Ce}$  ratios versus the source water content of oceanic basalts and arc melt inclusions. References: MORB [Michael, 1995], EM [Wallace, 2002; Workman et al., 2004, 2006; Dixon et al., 2008; Kendrick et al., 2014], HIMU [Cabral et al., 2014], Hawaii basalt [Dixon et al., 1997; Wallace, 1998; Dixon and Clague, 2001; Dixon et al., 2008], arc lava melt inclusions [Plank et al., 2009, 2013], Kaapvaal peridotites [Peslier et al., 2012], and Siberian craton peridotites [Doucet et al., 2014]. The  $\text{H}_2\text{O}/\text{Ce}$  ratio for the Kaapvaal peridotites is that of melts in equilibrium with the peridotites because no bulk Ce concentrations are available for these samples. The  $\text{H}_2\text{O}/\text{Ce}$  ratio for the Siberian peridotites uses a bulk Ce concentration calculated from the Ce contents of individual phases.

contained enough water to re-enrich the peridotites in water, but had to be overall relatively dry, as evidenced by mantle-melt interaction models ( $<1$  wt.%  $\text{H}_2\text{O}$ ; Figure 1) and the fact that melts in equilibrium with most Labait peridotite minerals contain  $<2$  wt.%  $\text{H}_2\text{O}$  (supporting information Table S4). This is surprising because most plume-related volcanism is characterized by magmas having water contents higher than MORB, which in turn translates into a more water-rich source compared to that of MORB (see Hawaii, EM and HIMU source water contents in Figure 11) [Wallace, 1998]. This suggests that either the plume beneath the EAR generates dry melts, or its melts are as wet as typical OIB and the peridotite refertilization process is decoupling water from other incompatible elements. The only water analyses of EAR lavas that we could find in the literature suggest high water contents, as exemplified by Kenyan rhyolites with pre-eruptive and predegassing water contents of up to 5.7 wt.%  $\text{H}_2\text{O}$  [Wilding et al., 1993].

Craton-plume interaction can be further examined by calculating the  $\text{H}_2\text{O}/\text{Ce}$  ratio of melts in equilibrium with the pyroxenes (Figure 11). Water and Ce are thought to behave similarly during melting/crystallization and the ratio in melts may be indicative of the tectonic setting [Michael, 1995; Plank et al., 2009]. The  $\text{H}_2\text{O}/\text{Ce}$  ratios of Labait peridotites are mostly lower than those of MORB [Michael, 1995] and of HIMU oceanic island basalts [Cabral et al., 2014]. The  $\text{H}_2\text{O}/\text{Ce}$  ratios of peridotites from Kaapvaal craton [Peslier et al., 2012] and Siberian craton [Doucet et al., 2014] extend to higher values compared to those of Labait, overlapping with the field for arc melt inclusions [Plank et al., 2009, 2013]. The Labait  $\text{H}_2\text{O}/\text{Ce}$  ratios are lower than those of Hawaiian basalts, except for those with EM affinity [Wallace, 1998; Dixon and Clague, 2001; Dixon et al., 2008; Bizimis and Peslier, 2015]. Labait peridotites are most similar to EM type basalts in terms of  $\text{H}_2\text{O}/\text{Ce}$  ratios [Wallace, 2002; Workman et al., 2004, 2006; Dixon et al., 2008; Kendrick et al., 2014]. This is consistent with the source of the EAR lavas having radiogenic and noble gas isotope components in their source similar to EM1 and HIMU oceanic basalts [Paslick et al., 1995; Bell and Tilton, 2001; Pik et al., 2006].

To summarize, water contents of olivine and orthopyroxene in the deepest xenoliths reflect refertilization by LREE and Fe-rich but relatively water-poor melts linked to the super plume. The shallowest lithosphere underwent cryptic metasomatism by the same melts. The absence of clear trends between water contents and other tracers in the shallower peridotites may be the result of an Archean mantle lithosphere that retained its original (relatively low) water content established by melting events 2.8–2.2 Ga ago. Two key

clinopyroxene between the two age groups (Figure 5g and 5h). The best scenario to explain our observations is infiltration of plume-derived Fe and LREE-rich melts that were introduced into the cratonic mantle by the super plume responsible for the rift [Rooney et al., 2012]. Additional evidence for this scenario comes from the microstructures of the deepest Labait peridotites, which are consistent with recrystallization that was possibly induced by melt infiltration [Vauchez et al., 2005]. Other Northern Tanzanian xenolith localities also show significant overprinting by plume-related melts that precipitated hydrous phases such as phlogopite and amphibole (e.g., Pello Hill and Eledo) [Dawson and Smith, 1988]. Consequently, the melts originating from the plume

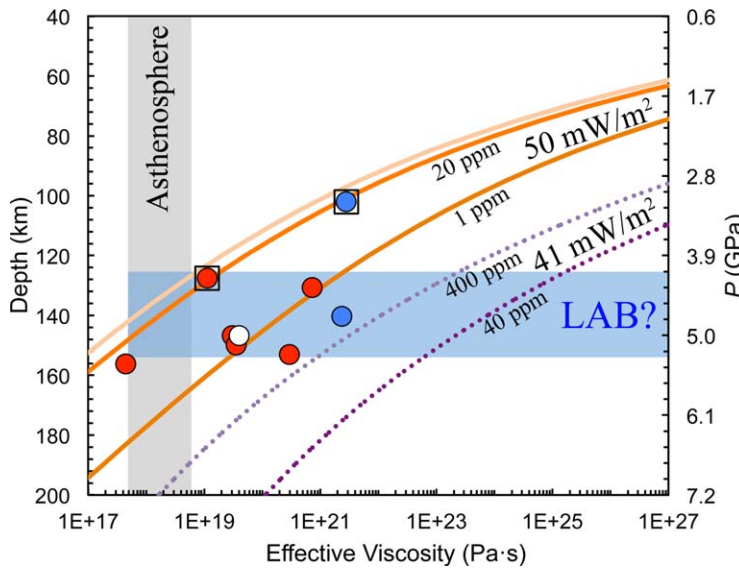


**Figure 12.** Calculated effective viscosity versus depth or pressure. Dotted lines show the effective viscosities for a typical cratonic geotherm calculated using a surface heat flow of  $41 \text{ mW/m}^2$  with different water contents (40 ppm and 400 ppm). Solid curves show the effective viscosities for a mantle geotherm calculated using a surface heat flow of  $50 \text{ mW/m}^2$  with different water contents (1, 20, and 40 ppm). Labait samples are shown by colored symbols (see Figure 2 for key). One data point for a mantle peridotite from Lashaine (open circle) in Baptiste et al. [2015] is plotted here for comparison. Details on the calculation can be found in the supporting information Text S1. The range of viscosity for asthenospheric mantle [Pollitz et al., 1998; Sjöberg et al., 2000; Larsen et al., 2005] and possible depths of the lithosphere and asthenosphere boundary (LAB) are also shown.

therefore water plays a key role in controlling mantle viscosity [Karato and Wu, 1993; Hirth and Kohlstedt, 1996]. The high olivine modal abundance ( $>60$  vol%) [Lee and Rudnick, 1999], together with the fact that its strength is less than that of pyroxene [e.g., Yamamoto et al., 2008], means that olivine likely controls deformation in mantle peridotites. It has been suggested that for a cratonic lithosphere to be stable, the olivine water content should be lower than  $\sim 10$  ppm  $\text{H}_2\text{O}$  [Katayama and Korenaga, 2011]. Most Labait olivines have less than 10 ppm  $\text{H}_2\text{O}$  (Table 2) and the Tanzanian mantle lithosphere is dry compared to that of other cratons (Kaapvaal and Siberian, Figures 2 and 11), which could have contributed to its long-term stability. However, mantle temperature exerts the largest influence on viscosity [e.g., Karato, 2010] and Labait mantle xenoliths generally record higher temperatures than those from other cratonic mantle lithospheres (Figure 2a).

Following Peslier et al. [2010], we calculated the effective viscosity of the lithospheric mantle beneath Labait using olivine water contents and xenolith-derived geotherms (Figure 12). The calculated viscosities of Labait peridotites (Figure 12) generally fall within the range of the mantle viscosity calculated with water content from 1 to 40 ppm  $\text{H}_2\text{O}$  and a geotherm with  $50 \text{ mW/m}^2$  heat flow [Lee and Rudnick, 1999], which is hotter than a typical cratonic geotherm ( $41 \text{ mW/m}^2$ ) [e.g., Rudnick et al., 1998]. The Tanzanian craton may have had a lower and more typical cratonic geotherm prior to interaction with the plume. Adding unreasonably high amounts of water (400 ppm  $\text{H}_2\text{O}$ ) to olivine to calculate viscosities for a typical cold cratonic peridotite (heat flow of  $41 \text{ mW/m}^2$ ) is not enough to match the low viscosities of the Labait xenoliths. This indicates that water at least has not played an important role in destruction of the cratonic mantle lithosphere. Only increasing the temperature (heat flow of  $50 \text{ mw/m}^2$  in Figure 12) can produce viscosity curves that match Labait peridotite viscosities. Indeed, the Tanzanian craton appears to be a strong block around which the rift split [Nyblade and Brazier, 2002], consistent with the low water contents observed in the Tanzanian xenoliths.

At Labait, the intersection of the conductive geotherm with the adiabat suggests that the lithospheric mantle there is thinner [Lee and Rudnick, 1999] compared to the lithospheric thickness at the center of the Tanzanian craton inferred from seismic data (up to  $\sim 7$  GPa) [Weeraratne et al., 2003] and garnet xenocrysts carried in 40 Ma kimberlites [Griffin et al., 1994]. Cratonic root stability is thought to require a viscosity ratio

observations result from this study: 1) Craton-plume interaction may not result in significant water enrichment of the cratonic lithosphere, and 2) The Tanzanian craton has one of the driest cratonic lithospheres yet analyzed (Figure 11) [cf. Peslier et al., 2012; Doucet et al., 2014].

### 5.6. Mantle Viscosity and Craton Stability

Laboratory deformation experiments have revealed that water plays an important role in controlling the viscosity of olivine, pyroxene, and garnet [Mackwell et al., 1985; Mei and Kohlstedt, 2000a, 2000b; Hier-Majumder et al., 2005; Chen et al., 2006; Katayama and Karato, 2008]. Water can weaken olivine, volumetrically the most abundant mineral in the mantle, and

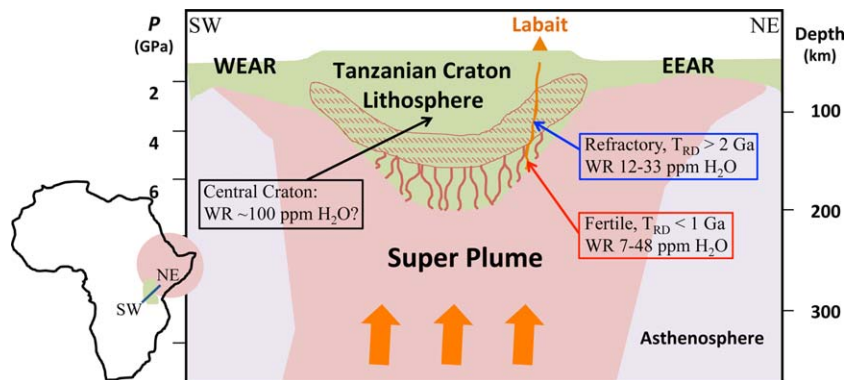


**Figure 13.** Simplified sketch of the Tanzanian craton lithosphere interacting with the mantle super plume. The water content of the central craton, inferred from electrical conductivity data, is from Selway et al. [2014]. Schematic cross section and present surface expression (location) of the super plume are based on Mulibio and Nyblade [2013] and Ebinger and Sleep [1998]. Thickness of the lithosphere is based on Griffin et al. [1994], Chesley et al. [1999] and Lee and Rudnick [1999]. The rhenium depletion ages ( $T_{RD}$ ) are from Chesley et al. [1999]. EEAR = eastern branch of the East African Rift, WEAR = western branch of the East African Rift.

between asthenosphere and lithosphere of at least 50 [O'Neill et al., 2008]. The viscosity range of the asthenosphere is  $5 \times 10^{17} - 5 \times 10^{18}$  Pa·s [Pollitz et al., 1998; Sjöberg et al., 2000; Larsen et al., 2005]. Our viscosity curves at 50 mW/m<sup>2</sup> and 1–20 ppm H<sub>2</sub>O in olivine, appropriate for the Labait lithospheric mantle, intersect the values of fifty times the highest asthenosphere viscosity estimate ( $\sim 2.5 \times 10^{19}$  Pa·s) between 4.1 and 5.3 GPa (Figure 12). These pressures could be taken as an estimation of the minimum depth of the lithosphere–asthenosphere boundary (LAB) beneath Labait (Figure 12). This relatively shallow LAB depth is either due to erosion by the super plume and replacement of cratonic lithosphere by plume material [e.g., Chesley et al., 1999; Weeraratne et al., 2003], or is due to the fact that Labait is located at the edge of the craton, which may be thinner than its center.

Water could play a significant role in cratonic root erosion via weakening of olivine, and this mechanism has been invoked to explain the relative thinness of the Colorado Plateau compared to other older cratons [Li et al., 2008]. At Labait, only a few of the deepest samples have viscosities close enough to that of the asthenosphere to allow convective removal (Figure 12). If the Tanzanian lithospheric mantle beneath Labait has been thinned, however, its low water contents and high temperatures are more consistent with thermal erosion than hydrolytic weakening (Figure 12). Our present study suggests that cratonic root erosion may not be linked to addition of water. The relative dryness of the plume-derived melts may be the reason why the Tanzanian craton has retained its mantle root, at least in its center, despite being underplated by one of the largest plumes seen in the Earth's mantle and completely surrounded by its expression at the surface, the East African Rift.

### 5.7. Water, Seismic Wave Attenuation and Electrical Conductivity Observations

Water in olivine may affect seismic wave attenuation through changes of olivine anisotropy [Karato, 2006; Shito et al., 2006]. The crystallographic preferred orientation (CPO) of Labait olivine, one measure of anisotropy, tends to increase with mantle depth [Vauchez et al., 2005], yet the olivines of both the shallow and deep xenolith groups contain similar amounts of water. The B-type fabric, whose development has been suggested to be facilitated by water, indicates a high mobility of grain boundaries and the polarization direction of the faster S wave [e.g., Jung and Karato, 2001]. Three of the samples from our study (LB45, LB53 and LB24) were shown by Vauchez et al. [2005] to exhibit axial [010] fabric. The olivines in these samples contain 30, 7 and  $\sim 1$  ppm H<sub>2</sub>O respectively (Table 2). Olivines in LB24, and in most Labait peridotites (10 out of 12; Table 2) contain significantly lower water concentrations than that necessary to induce fabric transitions in olivine (16 ppm H<sub>2</sub>O) [e.g., Jung and Karato, 2001; Skemer et al., 2013]. Therefore, our data do not support the hypothesis that water plays an important role in facilitating the development of seismic anisotropy in this region.

The interpretation of electrical conductivity data of the Tanzanian craton suggests that the Tanzanian cratonic lithosphere has a relatively dry edge but a wetter craton center [Selway et al., 2014]. Although no water measurement has been carried out on peridotite xenoliths from the center of the Tanzanian craton,

our data are consistent with a relatively dry craton edge. Furthermore, other cratons appear comparatively wet. The Kaapvaal craton has 13–135 ppm H<sub>2</sub>O [Peslier *et al.*, 2012] while the Siberian craton contains up to 300 ppm H<sub>2</sub>O [Doucet *et al.*, 2014] (Figure 11).

## 6. Conclusions

New water and trace element compositions are reported in NAMs from twelve peridotite xenoliths brought up by the Labait volcano, which samples a stratified lithosphere composed of ancient (>2 Ga), refractory peridotites to depth of ~130 km, underlain by more fertile, younger peridotites (<1 Ga) to ~160 km depth [Chesley *et al.*, 1999] (Figure 13). Water is homogenously distributed in olivine (1–39 ppm), orthopyroxene (10–150 ppm) and clinopyroxene (16–340 ppm) for each mantle xenolith, and is at the lower end of the range of water contents measured in cratonic mantle peridotites worldwide. Water contents overlap for the two age groups (Figure 13). The homogeneous distribution of water within olivines and pyroxenes suggests that their water contents reflect mantle values. By contrast, water is enriched on the rim of at least two garnets from sample LB24 (the only sample for which fresh garnet could be extracted), indicating that the host melilitite was hydrous. Diffusion modeling of the water profile preserved in one garnet indicates that the host olivine-melilitite ascended at a rate of 4–28 m/s.

In the >2 Ga peridotites, only orthopyroxene water contents correlate with indices of partial melting. In the <1 Ga peridotites, both olivine and orthopyroxene water contents correlate with indices of partial melting, yet the inferred melting depth is shallower than the equilibration depth of the xenoliths. Moreover, all water contents are too high to be explained by simple partial melting. The enhanced water contents, as well as trace element distribution patterns of clinopyroxenes in both age groups are consistent with overprinting by a LREE and Fe enriched, but relatively water-poor (<1 wt.% H<sub>2</sub>O) melt, likely related to the plume. Thus, plume-cratonic mantle interaction may not necessarily lead to significant enrichment in water of the cratonic mantle lithosphere.

The mantle lithosphere at Labait is thinner than at the center of the Tanzanian craton [Griffin *et al.*, 1994; Chesley *et al.*, 1999; Lee and Rudnick, 1999]. If this feature is the result of erosion/delamination linked to the plume, the low water contents (<50 ppm H<sub>2</sub>O) and the high temperatures recorded in the Labait peridotites indicate that high temperatures, rather than water, may be responsible for lowering the cratonic lithosphere viscosity and leading to its erosion. The fact that the Tanzanian craton has maintained its >200 km thick mantle root despite being located above a super plume and surrounded by the resulting active rifts may be linked to its low water content, which has not yet been significantly disturbed by refertilization by plume-derived melts.

## Acknowledgments

This project was supported by NSF grants EAR 0802652 and EAR 1118335 to AHP and EAR 9506510 to RLR. We thank Cin-Ty Lee for invaluable discussions. We are grateful for the comments from two anonymous reviewers that greatly improved the manuscript and for efficient editing by T. Becker. Supporting data are provided in the tables and figures, including those in an SI file.

## References

- Adams, A., A. Nyblade and D. Weeraratne (2012), Upper mantle shear wave velocity structure beneath the East African plateau: Evidence for a deep, plateau-wide low velocity anomaly, *Geophys. J. Int.*, **189**, 123–142.
- Aubaud, C., E. H. Hauri, and M. M. Hirschmann (2004), Hydrogen partition coefficients between nominally anhydrous minerals and basaltic melts, *Geophys. Res. Lett.*, **31**, L20611, doi:10.1029/2004GL021341.
- Aubaud, C., M. M. Hirschmann, A. C. Withers and R. L. Hervig (2008), Hydrogen partitioning between melt, clinopyroxene, and garnet at 3 GPa in a hydrous MORB with 6 wt.% H<sub>2</sub>O, *Contrib. Mineral. Petrol.*, **156**, 607–625.
- Aulbach, S., and R. L. Rudnick (2009), Origins of non-equilibrium lithium isotopic fractionation in xenolithic peridotite minerals: Examples from Tanzania, *Chem. Geol.*, **258**, 17–27.
- Aulbach, S., R. L. Rudnick, and W. F. McDonough (2008), Li-Sr-Nd isotope signatures of the plume and cratonic lithospheric mantle beneath the margin of the rifted Tanzanian craton (Labait), *Contrib. Mineral. Petrol.*, **155**, 79–92.
- Aulbach, S., R. L. Rudnick, and W. F. McDonough (2011), Evolution of the lithospheric mantle beneath the East African Rift in Tanzania and its potential signatures in rift magmas, *Geol. Soc. Am. Spec. Pap.*, **478**, 105–125.
- Baptiste, V., A. Tommasi, and S. Demouchy (2012), Deformation and hydration of the lithospheric mantle beneath the Kaapvaal craton, South Africa, *Lithos*, **149**, 31–50.
- Baptiste, V., A. Tommasi, A. Vauchez, S. Demouchy, and R. L. Rudnick (2015), Deformation, hydration, and anisotropy of the lithospheric mantle in an active rift: Constraints from mantle xenoliths from the North Tanzanian Divergence of the East African Rift, *Tectonophysics*, **639**, 34–55.
- Bell, D. R., and G. R. Rossman (1992a), Water in the earth's mantle: The role of nominally anhydrous minerals, *Science*, **255**, 1391–1397.
- Bell, D. R., and G. R. Rossman (1992b), The distribution of hydroxyl in garnets from the subcontinental mantle of southern Africa, *Contrib. Mineral. Petrol.*, **111**, 161–178.
- Bell, D. R., P. D. Ihinger, and G. R. Rossman (1995), Quantitative analysis of trace OH in garnet and pyroxenes, *Am. Mineral.*, **80**, 465–474.
- Bell, D. R., G. R. Rossman, J. Maldener, D. Endisch and F. Rauch (2003a), Hydroxide in olivine: A quantitative determination of the absolute amount and calibration of the IR spectrum, *J. Geophys. Res.*, **108(B5)**, 2105, doi:10.1029/2001JB000679.
- Bell, D. R., M. D. Schmitz, and P. E. Janney (2003b), Mesozoic thermal evolution of the southern African mantle lithosphere, *Lithos*, **71**, 273–287.

- Bell, K., and G. R. Tilton (2001), Nd, Pb and Sr isotopic compositions of East African carbonatites: Evidence for mantle mixing and plume inhomogeneity, *J. Petrol.*, 42, 1927–1945.
- Beuchert, M. J., Y. Y. Podladchikov, N. S. C. Simon, and L. H. Rüpke (2010), Modeling of craton stability using a viscoelastic rheology, *J. Geophys. Res.*, 115, B11413, doi:10.1029/2009JB006482.
- Bizimis, M., and A. H. Peslier (2015), Water in Hawaiian garnet pyroxenites: Implications for water heterogeneity in the mantle, *Chem. Geol.*, 397, 61–75.
- Blanchard, M., and J. Ingrin (2004), Hydrogen diffusion in Dora Maira pyrope, *Phys. Chem. Miner.*, 31, 593–605.
- Bonadiman, C., Y. Hao, M. Coltorti, L. Dallai, B. Faccini, Y. Huang, and Q. Xia (2009), Water contents of pyroxenes in intraplate lithospheric mantle, *Eur. J. Mineral.*, 21, 637–647.
- Brey, G. P., and T. Köhler (1990), Geothermobarometry in four-phase Iherzolites II. New thermobarometers, and practical assessment of existing thermobarometers, *J. Petrol.*, 31, 1353–1378.
- Burton, K. W., P. Schiano, J.-L. Birck, C. J. Allègre, M. Rehkämper, A. N. Halliday, and J. B. Dawson (2000), The distribution and behaviour of rhodium and osmium amongst mantle minerals and the age of the lithospheric mantle beneath Tanzania, *Earth Planet. Sci. Lett.*, 183, 93–126.
- Cabral, R. A., M. G. Jackson, K. T. Koga, E. F. Rose-Koga, E. H. Hauri, M. J. Whitehouse, A. A. Price, J. M. D. Day, N. Shimizu, and K. A. Kelley (2014), Volatile cycling of  $H_2O$ ,  $CO_2$ , F, and Cl in the HIMU mantle: A new window provided by melt inclusions from oceanic hot spot lavas at Mangaia, Cook Islands, *Geochim. Geophys. Geosyst.*, 15, 4445–4467, doi:10.1002/2014GC005473.
- Chen, S., T. Hiraga, and D. L. Kohlstedt (2006), Water weakening of clinopyroxene in the dislocation creep regime, *J. Geophys. Res.*, 111, B08203, doi:10.1029/2005JB003885.
- Chesley, J. T., R. L. Rudnick, and C.-T. Lee (1999), Re-Os systematics of mantle xenoliths from the East African Rift: Age, structure, and history of the Tanzanian craton, *Geochim. Cosmochim. Acta*, 63, 1203–1217.
- Cohen, R. S., R. K. O'Nions, and J. B. Dawson (1984), Isotope geochemistry of xenoliths from East Africa: Implications for development of mantle reservoirs and their interaction, *Earth Planet. Sci. Lett.*, 68, 209–220.
- Dawson, J. B. (1999), Metasomatism and melting in spinel peridotite xenoliths from Labait, Tanzania, *Proc. Int. Kimberlite Conf.*, 7, 164–173.
- Dawson, J. B. (2002), Metasomatism and partial melting in upper-mantle peridotite xenoliths from the Lashaine volcano, northern Tanzania, *J. Petrol.*, 43, 1749–1777.
- Dawson, J. B. (2008), The Gregory rift valley and neogene—Recent volcanoes of northern Tanzania, *Geol. Soc. Mem.*, 33, 1–98.
- Dawson, J. B. (2012), Nephelinite-mellilitite-carbonatite relationships: Evidence from Pleistocene – recent volcanism in northern Tanzania, *Lithos*, 152, 3–10.
- Dawson, J. B., and J. V. Smith (1988), Metasomatised and veined upper-mantle xenoliths from Pello Hill, Tanzania: Evidence for anomalously-light mantle beneath the Tanzanian sector of the East African Rift Valley, *Contrib. Mineral. Petrol.*, 100, 510–527.
- Dégi, J., R. Abart, K. Török, E. Bali, R. Wirth, and D. Rhede (2010), Symplectite formation during decompression induced garnet breakdown in lower crustal magic granulite xenoliths: Mechanisms and rates, *Contrib. Mineral. Petrol.*, 159, 293–314.
- Demouchy, S., S. D. Jacobsen, F. Gaillard, and C. R. Stern (2006), Rapid magma ascent recorded by water diffusion profiles in mantle olivine, *Geology*, 34, 429–432.
- DePaolo, D. J. (1981), Trace element and isotopic effects of combined wallrock assimilation and fractional crystallization, *Earth Planet. Sci. Lett.*, 53, 189–202.
- Dixon, J. E., and D. A. Clague (2001), Volatiles in basaltic glasses from Loihi seamount, Hawaii: Evidence for a relatively dry plume component, *J. Petrol.*, 42, 627–654.
- Dixon, J. E., D. A. Clague, P. J. Wallace and R. J. Poreda (1997), Volatiles in alkalic basalts from the North Arch Volcanic Field, Hawaii: Extensive degassing of deep submarine-erupted alkalic series lavas, *J. Petrol.*, 38, 911–939.
- Dixon, J. E., L. Leist, C. Langmuir, and J.-G. Schilling (2002), Recycled dehydrated lithosphere observed in plume-influenced mid-ocean-ridge basalt, *Nature*, 420, 385–389.
- Dixon, J. E., T. H. Dixon, D. R. Bell, and R. Malservisi (2004), Lateral variation in upper mantle viscosity: Role of water, *Earth Planet. Sci. Lett.*, 222, 451–467.
- Dixon, J. E., D. A. Clague, B. Cousens, M. L. Monslave, and J. Uhl (2008), Carbonatite and silicate melt metasomatism of the mantle surrounding the Hawaiian plume: Evidence from volatiles, trace elements, and radiogenic isotopes in rejuvenated-stage lavas from Niuhau, Hawaii, *Geochim. Geophys. Geosyst.*, 9, Q09005, doi:10.1029/2008GC002076.
- Doucet, L. S., A. H. Peslier, D. A. Ionov, A. D. Brandon, A. V. Golovin, A. G. Goncharov and I. V. Ashchepkov (2014), High water contents in the Siberian cratonic mantle linked to metasomatism: An FTIR study of Udachnaya peridotite xenoliths, *Geochim. Cosmochim. Acta*, 137, 159–187.
- Ebinger, C. J., and N. H. Sleep (1998), Cenozoic magmatism throughout east Africa resulting from impact of a single plume, *Nature*, 395, 788–791.
- Farver, J. R. (2010), Oxygen and hydrogen diffusion in minerals, *Rev. Mineral. Geochem.*, 72, 447–507.
- Gibson, S. A., S. C. McMahon, J. A. Day, and J. B. Dawson (2013), Highly refractory lithospheric mantle beneath the Tanzanian craton: Evidence from Lashaine pre-metasomatic garnet-bearing peridotites, *J. Petrol.*, 54, 1503–1546.
- Godard, G., and S. Martin (2000), Petrogenesis of kelyphites in garnet peridotites: A case study from the Ulten zone, *Italian Alps. J. Geodyn.*, 30, 117–145.
- Grant, K. J., J. Ingrin, J. P. Lorand, and P. Dumas (2007a), Water partitioning between mantle minerals from peridotite xenoliths, *Contrib. Mineral. Petrol.*, 154, 15–34.
- Grant, K. J., S. C. Kohn, and R. A. Brooker (2007b), The partitioning of water between olivine, orthopyroxene and melt synthesized in the system albite-forsterite- $H_2O$ , *Earth Planet. Sci. Lett.*, 260, 227–241.
- Griffin, W. L., C. G. Ryan, S. Y. O'Reilly, P. H. Nixon, and T. T. Win (1994), Trace elements in garnets from Tanzanian kimberlites: Relation to diamond content and tectonic setting, *Proc. Int. Kimberlite Conf.*, 5, 346–356.
- Hansen, S. E., A. A. Nyblade and M. H. Benoit (2012), Mantle structure beneath Africa and Arabia from adaptively parameterized P-wave tomography: Implications for the origin of Cenozoic Afro-Arabian tectonism, *Earth Planet. Sci. Lett.*, 319–320, 23–34.
- Hanson, R. E. (2003), Proterozoic geochronology and tectonic evolution of southern Africa, *Geol. Soc. Spec. Publ.*, 206, 427–463.
- Hao, Y., Q. Xia, Q. Li, H. Chen, and M. Feng (2014), Partial melting control of water contents in the Cenozoic lithospheric mantle of the Cathaysia block of South China, *Chem. Geol.*, 380, 7–19.
- Hauri, E. H., G. A. Gaetani, and T. H. Green (2006), Partitioning of water during melting of the Earth's upper mantle at  $H_2O$ -undersaturated conditions, *Earth Planet. Sci. Lett.*, 248, 715–734.
- Herzberg, C. (2004), Geodynamic information in peridotite petrology, *J. Petrol.*, 45, 2507–2530.
- Hier-Majumder, S., S. Mei, and D. L. Kohlstedt (2005), Water weakening of clinopyroxene in diffusion creep, *J. Geophys. Res.*, 110, B07406, doi:10.1029/2004JB003414.

- Hirschmann, M. M. (2006), Water, melting, and the deep Earth H<sub>2</sub>O cycle, *Ann. Rev. Earth Planet. Sci.*, 34, 629–653.
- Hirschmann, M. M., T. Tenner, C. Aubaud, and A. C. Withers (2009), Dehydration melting of nominally anhydrous mantle: The primacy of partitioning, *Phys. Earth Planet. Inter.*, 176, 54–68.
- Hirth, G., and D. L. Kohlstedt (1996), Water in the oceanic upper mantle: Implications for rheology, melt extraction and the evolution of the lithosphere, *Earth Planet. Sci. Lett.*, 144, 93–108.
- Ingrin, J., and M. Blanchard (2006), Diffusion of hydrogen in minerals, *Rev. Mineral. Geochem.*, 62, 291–320.
- Ionov, D. A., G. Chazot, C. Chauvel, C. Merlet, and J.-L. Bodinier (2006), Trace element distribution in peridotite xenoliths from Tok, SE Siberian craton: A record of pervasive, multi-stage metasomatism in shallow refractory mantle, *Geochim. Cosmochim. Acta*, 70, 1231–1260.
- Ionov, D. A., L. S. Doucet, and I. V. Ashchepkov (2010), Composition of the lithospheric mantle in the Siberian craton: New constraints from fresh peridotites in the Udachnaya-East kimberlite, *J. Petrol.*, 51, 2177–2210.
- James, D. E., F. R. Boyd, D. Schutt, D. R. Bell, and R. W. Carlson (2004), Xenolith constraints on seismic velocities in the upper mantle beneath southern Africa, *Geochem. Geophys. Geosyst.*, 5, Q01002, doi:10.1029/2003GC000551.
- Jordan, T. H. (1978), Composition and development of the continental tectosphere, *Nature*, 274, 544–548.
- Jung, H., and S. Karato (2001), Water-induced fabric transitions in olivine, *Science*, 293, 1460–1463.
- Karato, S. (2006), Remote sensing of hydrogen in Earth's mantle, *Rev. Mineral. Geochem.*, 62, 343–375.
- Karato, S. (2010), Rheology of the deep upper mantle and its implications for the preservation of the continental roots: A review, *Tectonophysics*, 481, 82–98.
- Karato, S., and P. Wu (1993), Rheology of the upper mantle: A synthesis, *Science*, 260, 771–778.
- Katayama, I., and S. Karato (2008), Effects of water and iron content on the rheological contrast between garnet and olivine, *Phys. Earth Planet. Inter.*, 166, 57–66.
- Katayama, I., and J. Korenaga (2011), Is the African cratonic lithosphere wet or dry?, *Geol. Soc. Am. Spec. Pap.*, 478, 249–256.
- Kendrick, M. A., M. J. Jackson, A. J. R. Kent, E. H. Hauri, P. J. Wallace and J. Woodhead (2014), Contrasting behaviours of CO<sub>2</sub>, S, H<sub>2</sub>O and halogens (F, Cl, Br, and I) in enriched-mantle melts from Pitcairn and Society seamounts, *Chem. Geol.*, 370, 69–81.
- Keppler, H., and N. Bolfan-Casanova (2006), Thermodynamics of water solubility and partitioning, *Rev. Mineral. Geochem.*, 62, 193–230.
- Kohn, S. C., and K. J. Grant (2006), The partitioning of water between nominally anhydrous minerals and silicate melts, *Rev. Mineral. Geochem.*, 62, 231–241.
- Koornneef, J. M., G. R. Davies, S. P. Döpp, Z. Vukmanovic, I. K. Nikogosian, and P. R. D. Mason (2009), Nature and timing of multiple metasomatic events in the sub-cratonic lithosphere beneath Labait, Tanzania, *Lithos*, 112S, 896–912.
- Kurka, A., M. Blanchard, and J. Ingrin (2005), Kinetics of hydrogen extraction and deuteration in grossular, *Mineral. Mag.*, 69, 359–371.
- Kurosawa, M., H. Yurimoto, and S. Sueno (1997), Patterns in the hydrogen and trace element compositions of mantle olivines, *Phys. Chem. Miner.*, 24, 385–395.
- Larsen, C. F., R. J. Motyka, J. T. Freymueller, K. A. Echelmeyer, and E. R. Ivins (2005), Rapid viscoelastic uplift in southeast Alaska caused by post-Little Ice Age glacial retreat, *Earth Planet. Sci. Lett.*, 237, 548–560.
- Lee, C.-T. (2005), Trace element evidence for hydrous metasomatism at the base of the North American lithosphere and possible association with Laramide low-angle subduction, *J. Geol.*, 113, 673–685.
- Lee, C.-T., and R. L. Rudnick (1999), Compositionally stratified cratonic lithosphere: Petrology and geochemistry of peridotite xenoliths from the Labait tuff cone, Tanzania, *Proc. Int. Kimberlite Conf.*, 7, 503–521.
- Lee, C.-T., P. Luffi, and E. J. Chin (2011), Building and destroying continental mantle, *Ann. Rev. Earth Planet. Sci.*, 39, 59–90.
- Lenardic, A., L.-N. Moresi, and H. Mühlhaus (2003), Longevity and stability of cratonic lithosphere: Insights from numerical simulations of coupled mantle convection and continental tectonics, *J. Geophys. Res.*, 108(B6), 2303, doi:10.1029/2002JB001859.
- Li, Z.-X., C.-T. Lee, A. H. Peslier, A. Lenardic, and S. J. Mackwell (2008), Water contents in mantle xenoliths from the Colorado Plateau and vicinity: Implications for the mantle rheology and hydration-induced thinning of continental lithosphere, *J. Geophys. Res.*, 113, B09210, doi:10.1029/2007JB005540.
- Mackwell, S. J., D. L. Kohlstedt, and M. S. Paterson (1985), The role of water in the deformation of olivine single crystals, *J. Geophys. Res.*, 90, 11,319–11,333.
- Manya, S., and M. A. H. Maboko (2003), Dating basaltic volcanism in the Neoarchaean Sukumaland Greenstone Belt of the Tanzania Craton using the Sm–Nd method: Implications for the geological evolution of the Tanzania Craton, *Precambrian Res.*, 121, 35–45.
- Manya, S., and M. A. H. Maboko (2008), Geochemistry and geochronology of Neoarchaean volcanic rocks of the Iramba–Sekenke greenstone belt, central Tanzania, *Precambrian Res.*, 163, 265–278.
- Manya, S., K. Kobayashi, M. A. H. Maboko, and E. Nakamura (2006), Ion microprobe zircon U–Pb dating of the late Archean metavolcanics and associated granites of the Musoma–Mara Greenstone Belt, Northeast Tanzania: Implications for the geological evolution of the Tanzanian Craton, *J. Afr. Earth Sci.*, 45, 355–366.
- Matsyuk, S., and K. Langer (2004), Hydroxyl in olivines from mantle xenoliths in kimberlites of the Siberian platform, *Contrib. Mineral. Petrol.*, 147, 413–437.
- Matsyuk, S., K. Langer, and A. Hösch (1998), Hydroxyl defects in garnets from mantle xenoliths in kimberlites of the Siberian platform, *Contrib. Mineral. Petrol.*, 132, 163–179.
- Mattsson, H. B. (2012), Rapid magma ascent and short durations in the Lake Natron–Engaruka monogenetic volcanic field (Tanzania): A case study of the olivine melilititic Pello Hill scoria cone, *J. Volcanol. Geotherm. Res.*, 247–248, 16–25.
- McDonough, W. F., and S.-S. Sun (1995), The composition of the Earth, *Chem. Geol.*, 120, 223–253.
- McDonough, W. F., H.-G. Stosch, and N. G. Ware (1992), Distribution of titanium and the rare earth elements between peridotite minerals, *Contrib. Mineral. Petrol.*, 110, 321–328.
- McNutt, M. K. (1998), Superswells, *Rev. Geophys.*, 36, 211–244.
- Mei, S., and D. L. Kohlstedt (2000a), Influence of water on plastic deformation of olivine aggregates 1. Diffusion creep regime, *J. Geophys. Res.*, 105, 21,457–21,469.
- Mei, S., and D. L. Kohlstedt (2000b), Influence of water on plastic deformation of olivine aggregates 2. Dislocation creep regime, *J. Geophys. Res.*, 105, 21,471–21,481.
- Messiga, B., and E. Bettini (1990), Reactions behaviour during kelyphite and symplectite formation: A case study of mafic granulites and eclogites from the Bohemian Massif, *Eur. J. Mineral.*, 2, 125–144.
- Michael, P. (1988), The concentration, behavior and storage of H<sub>2</sub>O in the suboceanic upper mantle: Implications for mantle metasomatism, *Geochim. Cosmochim. Acta*, 52, 555–566.
- Michael, P. (1995), Regionally distinctive sources of depleted MORB: Evidence from trace elements and H<sub>2</sub>O, *Earth Planet. Sci. Lett.*, 131, 301–320.

- Miller, G. H., G. R. Rossman, and G. E. Harlow (1987), The natural occurrence of hydroxyl in olivine, *Phys. Chem. Miner.*, 14, 461–472.
- Möller, A., P. Appel, K. Mezger, and V. Schenk (1995), Evidence for a 2 Ga subduction zone: Eclogites in the Usagaran belt of Tanzania, *Geology*, 23, 1067–1070.
- Mookherjee, M., and S.-I. Karato (2010), Solubility of water in pyrope-rich garnet at high pressures and temperature, *Geophys. Res. Lett.*, 37, L03310, doi:10.1029/2009GL041289.
- Mosenfelder, J. L., and G. R. Rossman (2013a), Analysis of hydrogen and fluorine in pyroxenes: I. Orthopyroxene, *Am. Mineral.*, 98, 1026–1041.
- Mosenfelder, J. L., and G. R. Rossman (2013b), Analysis of hydrogen and fluorine in pyroxenes: II. Clinopyroxene, *Am. Mineral.*, 98, 1042–1054.
- Mosenfelder, J. L., N. I. Deligne, P. D. Asimow, and G. R. Rossman (2006), Hydrogen incorporation in olivine from 2–12 GPa, *Am. Mineral.*, 91, 285–294.
- Mulibio, G. D., and A. A. Nyblade (2013), Mantle transition zone thinning beneath eastern Africa: Evidence for a whole-mantle superplume structure, *Geophys. Res. Lett.*, 40, 3562–3566.
- Norman, M. D. (1998), Melting and metasomatism in the continental lithosphere: Laser ablation ICPMS analysis of minerals in spinel lherzolites from eastern Australia, *Contrib. Mineral. Petrol.*, 130, 240–255.
- Novella, D., D. J. Frost, E. H. Hauri, H. Bureau, C. Raepsaet, and M. Roberge (2014), The distribution of H<sub>2</sub>O between silicate melt and nominally anhydrous peridotite and the onset of hydrous melting in the deep upper mantle, *Earth Planet. Sci. Lett.*, 400, 1–13.
- Nyblade, A. A. (2011), The upper-mantle low-velocity anomaly beneath Ethiopia, Kenya, and Tanzania: Constraints on the origin of the African superswell in eastern Africa and plate versus plume models of mantle dynamics, *Geol. Soc. Am. Spec. Pap.*, 478, 37–50.
- Nyblade, A. A. and R. A. Brazier (2002), Precambrian lithospheric controls on the development of the East African rift system, *Geology*, 30, 755–758.
- Nyblade, A. A., T. J. Owens, H. Gurrola, J. Ritsema, and C. A. Langston (2000), Seismic evidence for a deep upper mantle thermal anomaly beneath East Africa, *Geology*, 28, 599–602.
- O'Leary, J. A., G. A. Gaetani, and E. H. Hauri (2010), The effect of tetrahedral Al<sup>3+</sup> on the partitioning of water between clinopyroxene and silicate melt, *Earth Planet. Sci. Lett.*, 297, 111–120.
- O'Neill, C. J., A. Lenardic, W. L. Griffin, and S. Y. O'Reilly (2008), Dynamics of cratons in an evolving mantle, *Lithos*, 102, 12–24.
- O'Reilly, S. Y., and W. L. Griffin (2013), Mantle metasomatism, in *Metasomatism and the Chemical Transformation of Rock*, edited by D. E. Harlov and H. Austrheim, *Lect. Notes Earth Syst. Sci.*, pp. 471–533, Springer-Verlag, Berlin/Heidelberg.
- Palme, H., and H. St. C. O'Neill (2007), Cosmochemical estimates of mantle composition, *Treatise Geochem.*, 2, 1–38.
- Paslick, C., A. Halliday, D. James, and J. B. Dawson (1995), Enrichment of the continental lithosphere by OIB melts: Isotopic evidence from the volcanic province of northern Tanzania, *Earth Planet. Sci. Lett.*, 130, 109–126.
- Peslier, A. H. (2010), A review of water contents of nominally anhydrous natural minerals in the mantles of Earth, Mars and the Moon, *J. Volcanol. Geotherm. Res.*, 197, 239–258.
- Peslier, A. H., and J. F. Luhr (2006), Hydrogen loss from olivines in mantle xenoliths from Simcoe (USA) and Mexico: Mafic alkalic magma ascent rates and water budget of the sub-continental lithosphere, *Earth Planet. Sci. Lett.*, 242, 302–319.
- Peslier, A. H., J. F. Luhr, and J. Post (2002), Low water contents in pyroxenes from spinel-peridotites of the oxidized, sub-arc mantle wedge, *Earth Planet. Sci. Lett.*, 201, 69–86.
- Peslier, A. H., A. B. Woodland, and J. A. Wolff (2008), Fast kimberlite ascent estimated from hydrogen diffusion profiles in xenolithic mantle olivines from southern Africa, *Geochim. Cosmochim. Acta*, 72, 2711–2722.
- Peslier, A. H., A. B. Woodland, D. R. Bell, and M. Lazarov (2010), Olivine water contents in the continental lithosphere and the longevity of cratons, *Nature*, 467, 78–81.
- Peslier, A. H., A. B. Woodland, D. R. Bell, and M. Lazarov (2012), Metasomatic control of water contents in the Kaapvaal cratonic mantle, *Geochim. Cosmochim. Acta*, 97, 213–246.
- Peslier, A. H., M. Bizimis, and M. Matney (2015), Water disequilibrium in olivines from Hawaiian peridotites: Recent metasomatism, H diffusion and magma ascent rates, *Geochim. Cosmochim. Acta*, 154, 98–117. doi:10.1016/j.gca.2015.01.030.
- Pik, R., B. Marty, and D. R. Hilton (2006), How many mantle plumes in Africa? The geochemical point of view, *Chem. Geol.*, 226, 100–114.
- Plank, T., L. B. Cooper, and C. E. Manning (2009), Emerging geothermometers for estimating slab surface temperatures, *Nat. Geosci.*, 2, 611–615.
- Plank, T., K. A. Kelley, M. M. Zimmer, E. H. Hauri, and P. J. Wallace (2013), Why do mafic magmas contain ~4 wt% water on average?, *Earth Planet. Sci. Lett.*, 364, 168–179.
- Pollack, H. N. (1986), Cratonization and thermal evolution of the mantle, *Earth Planet. Sci. Lett.*, 80, 175–182.
- Pollitz, F. F., R. Bürgmann, and B. Romanowicz (1998), Viscosity of oceanic asthenosphere inferred from remote triggering of earthquakes, *Science*, 280, 1245–1249.
- Rampone, E., P. Bottazzi, and L. Ottolini (1991), Complementary Ti and Zr anomalies in orthopyroxene and clinopyroxene from mantle peridotites, *Nature*, 354, 518–520.
- Reid, A. M., and J. B. Dawson (1972), Olivine-garnet reaction in peridotites from Tanzania, *Lithos*, 5, 115–124.
- Ritsema, J., A. A. Nyblade, T. J. Owens, C. A. Langston, and J. C. VanDecar (1998), Upper mantle seismic velocity structure beneath Tanzania, East Africa: Implications for the stability of cratonic lithosphere, *J. Geophys. Res.*, 103, 21,201–21,213.
- Rooney, T. O., C. Herzberg and I. D. Bastow (2012), Elevated mantle temperature beneath East Africa, *Geology*, 40, 27–30.
- Rossman, G. R. (2006), Analytical methods for measuring water in nominally anhydrous minerals, *Rev. Mineral. Geochem.*, 62, 1–28.
- Rudnick, R. L., W. F. McDonough, and B. W. Chappell (1993), Carbonatite metasomatism in the northern Tanzanian mantle: Petrographic and geochemical characteristics, *Earth Planet. Sci. Lett.*, 114, 463–475.
- Rudnick, R. L., W. F. McDonough, and A. Orpin (1994), Northern Tanzanian peridotite xenoliths: A comparison with Kaapvaal peridotites and inferences on metasomatic interactions, *Proc. Int. Kimberlite Conf.*, 5, 336–353.
- Rudnick, R. L., W. F. McDonough, and R. J. O'Connell (1998), Thermal structure, thickness and composition of continental lithosphere, *Chem. Geol.*, 143, 395–411.
- Rudnick, R. L., T. R. Ireland, G. Gehrels, A. J. Irving, J. T. Chesley, and J. M. Hanchar (1999), Dating mantle metasomatism: U-Pb geochronology of cratonic mantle xenoliths from Montana and Tanzania, *Proc. Int. Kimberlite Conf.*, 7, 728–735.
- Sanislav, I. V., R. J. Wormald, P. H. G. M. Dirks, T. G. Blenkinsop, L. Salamba, and D. Joseph (2014), Zircon U-Pb ages and Lu-Hf isotope systematics from late-tectonic granites, Geita greenstone belt: Implications for crustal growth of the Tanzanian craton, *Precambrian Res.*, 242, 187–204.

- Schmädicke, E., J. Gose, and T. M. Will (2011), Heterogeneous mantle underneath the North Atlantic: Evidence from water in orthopyroxene, mineral composition and equilibrium conditions of spinel peridotite from different locations at the Mid-Atlantic Ridge, *Lithos*, 125, 308–320.
- Selway, K., J. Yi, and S.-I. Karato (2014), Water content of the Tanzanian lithosphere from magnetotelluric data: Implications for cratonic growth and stability, *Earth Planet. Sci. Lett.*, 388, 175–186.
- Shaw, D. M. (1979), Trace element melting models, *Phys. Chem. Earth*, 11, 577–586.
- Shito, A., S.-i. Karato, K. N. Matsukage and Y. Nishihara (2006), Towards mapping the three-dimensional distribution of water in the upper mantle from velocity and attenuation tomography, *Geophys. Monog. Ser.*, 168, 225–236.
- Sjöberg, L. E., M. Pan, E. Asenjo, and S. Erlingsson (2000), Glacial rebound near Vatnajökull, Iceland, studied by GPS campaigns in 1992 and 1996, *J. Geodyn.*, 29, 63–70.
- Skemer, P., J. M. Warren, L. N. Hansen, G. Hirth, and P. B. Kelemen (2013), The influence of water and LPO on the initiation and evolution of mantle shear zones, *Earth Planet. Sci. Lett.*, 375, 222–233.
- Skogby, H., D. R. Bell, and G. R. Rossman (1990), Hydroxide in pyroxene: Variations in the natural environment, *Am. Mineral.*, 75, 764–774.
- Smyth, J. R. (2006), Hydrogen in high pressure silicate and oxide mineral structures, *Rev. Mineral. Geochem.*, 62, 85–115.
- Sparks, R. S. J., L. Baker, R. J. Brown, M. Field, J. Schumacher, G. Stripp, and A. Walters (2006), Dynamical constraints on kimberlite volcanism, *J. Volcanol. Geotherm. Res.*, 155, 18–48.
- Spera, F. J. (1980), Aspects of magma transport, in *Physics of Magmatic Processes*, edited by R. B. Hargraves, pp. 265–323, Princeton Univ. Press, Princeton, N. J.
- Sundvall, R., and R. Stalder (2011), Water in upper mantle pyroxene megacrysts and xenocrysts: A survey study, *Am. Mineral.*, 96, 1215–1227.
- Tenczer, V., H. Fritz, A. Bauernhofer, and C. Hauzenberger (2007), Two orogens—One shear belt: 1 Ga of repeated deformation along the central Tanzanian shear belt, *J. Struct. Geol.*, 29, 1632–1649.
- Tenner, T. J., M. M. Hirschmann, A. C. Withers, and R. L. Hervig (2009), Hydrogen partitioning between nominally anhydrous upper mantle minerals and melt between 3 and 5 GPa and applications to hydrous peridotite partial melting, *Chem. Geol.*, 262, 42–56.
- Thomas, R. J., N. M. W. Roberts, J. Jacobs, A. M. Bushi, M. S. A. Horstwood, and A. Mruma (2013), Structural and geochronological constraints on the evolution of the eastern margin of the Tanzania Craton in the Mpwapwa area, central Tanzania, *Precambrian Res.*, 224, 671–689.
- Vauchez, A., F. Dineur, and R. L. Rudnick (2005), Microstructure, texture and seismic anisotropy of the lithospheric mantle above a mantle plume: Insights from the Labait volcano xenoliths (Tanzania), *Earth Planet. Sci. Lett.*, 232, 295–314.
- Walker, R. J., R. W. Carlson, S. B. Shirey, and F. R. Boyd (1989), Os, Sr, Nd, and Pb isotope systematics of southern African peridotite xenoliths: Implications for the chemical evolution of subcontinental mantle, *Geochim. Cosmochim. Acta*, 53, 1583–1595.
- Wallace, P. J. (1998), Water and partial melting in mantle plumes: Inferences from the dissolved H<sub>2</sub>O concentrations of Hawaiian basaltic magmas, *Geophys. Res. Lett.*, 25, 3639–3642.
- Wallace, P. J. (2002), Volatiles in submarine basaltic glasses from the northern Kerguelen plateau (ODP site 1140): Implications for source region compositions, magmatic processes, and plateau subsidence, *J. Petrol.*, 43, 1311–1326.
- Walter, M. J. (1998), Melting of garnet peridotite and the origin of komatiite and depleted lithosphere, *J. Petrol.*, 39, 29–60.
- Wang, L., Y. Zhang, and E. J. Essene (1996), Diffusion of the hydrous component in pyrope, *Am. Mineral.*, 81, 706–718.
- Wang, R., and B. Zhang (2011), Water in peridotite xenoliths from South China, *Sci. China Earth Sci.*, 54, 1511–1522.
- Weeraratne, D. S., D. W. Forsyth, K. M. Fischer, and A. A. Nyblade (2003), Evidence for an upper mantle plume beneath the Tanzania craton from Rayleigh wave tomography, *J. Geophys. Res.*, 108(B9), 2427, doi:10.1029/2002JB00273.
- Wilding, M. C., R. Macdonald, J. E. Davies, and A. E. Fallick (1993), Volatile characteristics of peralkaline rhyolites from Kenya: An ion microprobe, infrared spectroscopic and hydrogen isotope study, *Contrib. Mineral. Petrol.*, 114, 264–265.
- Withers, A. C., H. Bureau, C. Raepsaet, and M. M. Hirschmann (2012), Calibration of infrared spectroscopy by elastic recoil detection analysis of H in synthetic olivine, *Chem. Geol.*, 334, 92–98.
- Wölbern, I., G. Rümpker, K. Link, and F. Sodoudi (2012), Melt infiltration of the lower lithosphere beneath the Tanzania craton and the Albertine rift inferred from S receiver functions, *Geochim. Geophys. Geosyst.*, 13, Q0AK08, doi:10.1029/2012GC004167.
- Workman, R. K., S. R. Hart, M. Jackson, M. Regelous, K. A. Farley, J. Blusztajn, M. Kurz, and H. Staudigel (2004), Recycled metasomatized lithosphere as the origin of the Enriched Mantle II (EM2) end-member: Evidence from the Samoan Volcanic Chain, *Geochim. Geophys. Geosyst.*, 5, Q04008, doi:10.1029/2003GC000623.
- Workman, R. K., E. Hauri, S. R. Hart, J. Wang, and J. Blusztajn (2006), Volatile and trace elements in basaltic glasses from Samoa: Implications for water distribution in the mantle, *Earth Planet. Sci. Lett.*, 241, 932–951.
- Xia, Q.-K., Y. Hao, P. Li, E. Deloule, M. Coltorti, L. Dallai, X. Yang, and M. Feng (2010), Low water content of the Cenozoic lithospheric mantle beneath the eastern part of the North China Craton, *J. Geophys. Res.*, 115, B07207, doi:10.1029/2009JB006694.
- Xia, Q.-K., Y.-T. Hao, S.-C. Liu, X.-Y. Gu, and M. Feng (2013), Water contents of the Cenozoic lithospheric mantle beneath the western part of the North China Craton: Peridotite xenolith constraints, *Gondwana Res.*, 23, 108–118.
- Yamamoto, J., J.-i. Ando, H. Kagi, T. Inoue, A. Yamada, D. Yamazaki, and T. Irfune (2008), In situ strength measurements on natural upper-mantle minerals, *Phys. Chem. Miner.*, 35, 249–257.
- Yang, X.-Z., Q.-K. Xia, E. Deloule, L. Dallai, Q.-C. Fan, and M. Feng (2008), Water in minerals of the continental lithospheric mantle and overlying lower crust: A comparative study of peridotite and granulite xenoliths from the North China Craton, *Chem. Geol.*, 256, 33–45.
- Yu, Y., X.-S. Xu, W. L. Griffin, S. Y. O'Reilly, and Q.-K. Xia (2011), H<sub>2</sub>O contents and their modification in the Cenozoic subcontinental lithospheric mantle beneath the Cathaysia block, SE China, *Lithos*, 126, 182–197.
- Zhang, Y. (2010), Diffusion in minerals and melts: Theoretical background, *Rev. Mineral. Geochem.*, 72, 5–59.
- Zhao, Y.-H., S. B. Ginsberg, and D. L. Kohlstedt (2004), Solubility of hydrogen in olivine: Dependence on temperature and iron content, *Contrib. Mineral. Petrol.*, 147, 155–161.